Search for compressed scalar top quark pairs in p-p collisions at LHC at $\sqrt{s} = 13$ TeV

A Thesis

submitted to
Indian Institute of Science Education and Research Pune
in partial fulfillment of the requirements for the
BS-MS Dual Degree Programme

by

Prachi Atmasiddha
Registration No: 20121088

Indian Institute of Science Education and Research Pune
Dr. Homi Bhabha Road,
Pashan, Pune 411008, INDIA.

May, 2017

Supervisor: Prof. Seema Sharma, Assistant Professor, IISER Pune

Certificate

This is to certify that this dissertation entitled **Search for compressed scalar top quark pairs in p-p collisions at LHC at $\sqrt{s} = 13$ TeV** towards the partial fulfilment of the BS-MS dual degree programme at the Indian Institute of Science Education and Research, Pune represents study/work carried out by Prachi Atmasiddha at Indian Institute of Science Education and Research under the supervision of Prof. Seema Sharma, Professor, Department of Physics , during the academic year 2016-2017.

29/03/2017

Prof. Seema Sharma

Prachi Atmasiddha

Committee:

Prof. Seema Sharma

Prof. Ritesh Singh

This thesis is dedicated to my parents Mr. Arvind Atmasiddha and Mrs. Jayashree Atmasiddha, my grandmother Mrs. Suhasini Gajanan Saraf and my uncle Mr. Shekhar Gajanan Saraf, who have always been supportive throughout my life.

Declaration

I hereby declare that the matter embodied in the report entitled **Search for compressed scalar top quark pairs in p-p collisions at LHC at $\sqrt{s} = 13$ TeV** are the results of the work carried out by me at the Department of Physics, Indian Institute of Science Education and Research, Pune, under the supervision of Prof. Seema Sharma and the same has not been submitted elsewhere for any other degree.

29/03/2017

Prachi Atmasiddha

Prof. Seema Sharma

Acknowledgements

It was a memorable experience for me to work on the thesis presented here. I became familiar with the methodology of research through this project. I am extremely grateful to my supervisor, Prof. Seema Sharma, IISER Pune, for her help, guidance, resources and support I received throughout the work. I learned a lot about physics at the LHC and the techniques used for the analyses through the discussions with her. I also sincerely extend my gratitude towards the DST-Inspire programme (by the Department of Science and Technology, Government of India), for providing financial support throughout my study at IISER Pune and also for sponsoring a poster presentation in CMS international collaboration meeting held at TIFR in Nov 2016. I would also like to thank the Physics department for providing resources required for the project work and also to the IT department of IISER Pune for putting efforts in the installation of the IISER Pune CMS cluster and resolving other technical issues related to the internet access whenever required. I am thankful to Dr. Hongxuan Liu from Baylor University, Texas, for the discussions of the details of the ongoing CMS searches and providing suggestions regarding my work. I thank TIFR computing support including Mr. Brij Jashal and Mr. Puneet Patel for the help they provided me in creating IndiaCMS account and also in fixing the computing issues whenever necessary. I am thankful to Prof. Ritesh Singh, IISER Kolkata, for agreeing to be one of the mentors in my thesis advisory committee, for evaluating the progress of the thesis till mid term and for providing references for further studies. I thank Prof. Sourabh Dube for the weekly physics discussions in the CMS group meetings. My group-mates Shubham Pandey, Irene Dutta, Shubhanshu Chauhan, Vinay Hegde, Aditee Rane, Divya Gadkari, Kunal Kothekar, Anshul Kapoor, Angira Rastogi have helped me in

my understanding of the physics and technical aspects of the work. The role of my family and friends has been very crucial throughout the project, as they motivated me throughout my work.

Abstract

Supersymmetry (SUSY) is one of the most appealing theories, which tries to explain some of the experimental and theoretical shortcomings of the Standard Model. It tries to solve the Hierarchy problem by introducing new particles (supersymmetric partners of the Standard Model particles). The quantum corrections due to these particles cancel the divergent contribution from the SM particles to the Higgs mass calculation. The top quark couples to the Higgs maximally due to its higher mass. Therefore, particularly, the supersymmetric partner of the top quark- scalar top quark (stop) is interesting for the searches to stabilize the Higgs mass.

It is not easy to single out a model in supersymmetry due to the large number of free parameters. So, theorists have come up with some simplified models, which can be tested experimentally. This thesis is based on one of such models, where a stop decays to a top quark and a neutralino, where neutralino is assumed to be the Lightest Supersymmetric Particle (LSP). It is weakly interacting and stable. Hence, it does not leave any trace in the detector contributing to the missing transverse energy (MET) in the event. This additional source of MET differentiates the signature of $t\bar{t}$ background from the signature of the signal $\tilde{t}\tilde{t}^*$ events.

Some of the popular MET based analyses have been successful in excluding stop particles up to the mass of 900 GeV. But, the lower mass regions still have weaker exclusion limits. Especially, the region in the stop-LSP mass plane described by $M_{\tilde{t}} \approx M_t + M_{\tilde{\chi}_1^0}$, contains some model points with lower stop masses, which have not been excluded yet due to the limitations of the current MET based searches. By selecting only the events with a hard ISR (Initial State Radiation) jet, the MET of the entire system can be improved and also the lower mass models can be probed. For the events produced using the Monte Carlo simulations, expected upper limits at 95% confidence level were calculated for the integrated luminosity $\mathscr{L} = 30$ fb^{-1}, 35.9 fb^{-1} and 100 fb^{-1} at $\sqrt{s} = 13$ TeV of centre of mass energy. These limits exclude stop masses in the range $225 \leqslant M_{\tilde{t}} < 450$. For the lower masses of LSP, another technique based on the fermionic and bosonic nature of the t and $\tilde{t}$, respectively, is used to study the effect of the spin correlations between the decay products of the top or stop pair produced. A dileptonanalysis can be used to study $\Delta\phi(l_1,l_2)$ distributions (l_1 and l_2 are the two leptons) and calculating the limits using the events in $\Delta\phi(l_1,l_2)$ bins, give better exclusion potential for the models with $M_{\tilde{t}} < 225$ GeV compared to that given by the full hadronic ISR tagging analysis.

Contents

List of Tables

List of Figures

Chapter 1

Introduction

1.1 Standard Model and its limitations

The Standard Model (SM) is the most successful theory of the physics of elementary particles to date [1] [2] [3]. Many predictions of this theoretical model have been experimentally verified with good precision. The SM is based on the basic formalism of quantum field theory. It describes the strong, weak and electromagnetic interactions between the fundamental particles, but it does not incorporate the gravitational interaction. All these interactions (field transformations) are described using the SU(3) × SU(2) × U(1) local gauge symmetry group, where the strong force is based on SU(3) symmetry group and the electroweak force is based on the SU(2) × U(1) symmetry group. The total number of generators associated with this model are 8+3+1, where each of these is associated with a vector boson. The eight gluons, which are massless spin-1 particles mediate the strong force (Quantum Chromodynamics). The four vector-fields, which mediate the electroweak forces are W^+, W^-, W^0 and B. The interaction of the scalar Higgs field with these vector-fields causes the spontaneous symmetry breaking [4] [5] [6] [7] [8] of the S(2) × U(1) symmetry group. This results in the three massive gauge bosons, W^+, W^-, and Z, and a massless γ boson and it also implies the existence of a neutral scalar boson, which is called the Higgs boson. It has been discovered at the LHC [9] [10] in 2012 making the Standard Model a success to a great extent. γ mediates the electromagnetic interactions and the massive bosons are responsible for mediating weak interactions.

Along with the bosons, there are three generations of leptons and quarks in the SM, which are all spin-$\frac{1}{2}$ particles. Each generation of leptons has an electrically charged member ($e^{\pm}$, $\mu^{\pm}$, $\tau^{\pm}$) and a corresponding neutral particle, called neutrino. The neutrinos are massless and can interact only via weak interactions in the SM. The quarks carry a colour charge and interact via strong interaction mediated by the gluons. All the fermions and massive bosons can interact with the Higgs boson and the strength of interaction depends on the masses of the particles (so massless particles do not couple to the Higgs).

Although being a successful theory, the SM has several inadequacies, some of which are explained in the following:

1. Higgs mass prediction: The recent discovery of the Higgs boson [9] [10] of mass 125 GeV at the LHC marks a major success of the SM. However, as Higgs couples to all the massive particles, theoretical quantum corrections to the Higgs has an additive effect on the Higgs mass in a divergent way and these corrections can reach up to the Planck scale. This is in contradiction with what we have observed experimentally.

2. Dark Matter: The SM does not have any explanation or a particle candidate, which explains the presence of dark matter inferred by the astrophysicists. [11]

3. The matter-antimatter asymmetry: Every particle has an anti-particle in the SM, with the same mass, but opposite electric charge. The observed matter-antimatter asymmetry in the universe could not be explained using the CP violation predicted by the SM. [12]

4. Massive neutrinos: The neutrinos are fairly established to be massive as inferred from the observation of neutrino oscillations [13] [14].

1.2 Introduction to supersymmetry

Many theories have been formulated to extend the SM to overcome its limitations. One of the most compelling extensions is the theory of Supersymmetry (SUSY). This theory proposes a superpartner for every SM particle, which is identical in every respect except it differs by a spin-$\frac{1}{2}$. The SUSY can be depicted as a transformation Q that converts bosonic fields to fermionic fields and vice versa.

$$Q|boson\rangle = |fermion\rangle \tag{1.1}$$

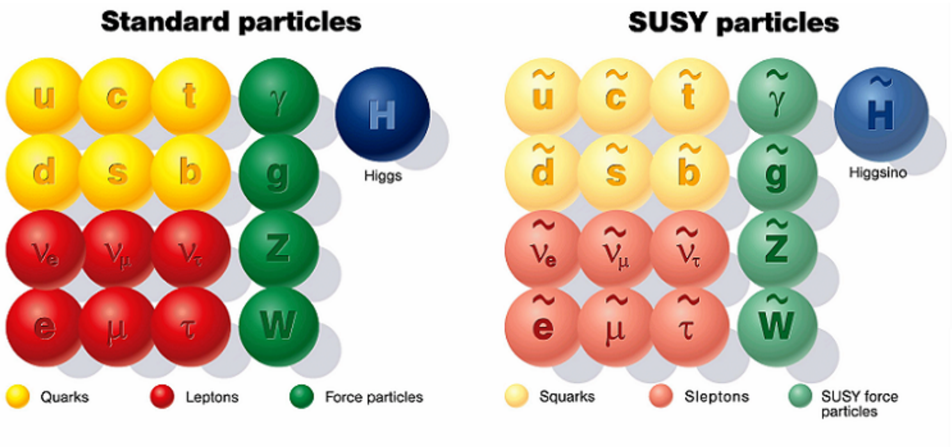

Figure 1.1: Standard Model particles on the left hand side and supersymmetric partners on the right hand side. [15]

The fermions and bosons contribute to the quantum corrections (illustrated in figure 1.2) to the Higgs mass with opposite signs. Therefore, the proposed superpartners of the SM particles exactly cancel the contributions to the Higgs boson mass, making it finite. The mass correction contribution due to a fermion:

$$\Delta M_H^2 = -\frac{|\lambda_f|^2}{8\pi^2}\Lambda_{UV}^2 + \ldots \tag{1.2}$$

The mass correction contribution due to the bosonic superpartners introduced in supersymmetry:

$$\Delta M_H^2 = \frac{\lambda_S}{8\pi^2}\Lambda_{UV}^2 + ... \tag{1.3}$$

Here, ΔM_H^2 is the quantum correction to Higgs mass squared, λ_f is the Yukawa coupling for a fermion, Λ_{UV}^2 is called the Ultraviolet cutoff and if $\lambda_S = |\lambda_f|^2$, then the contributions due to fermions cancel out with those of the corresponding bosons.

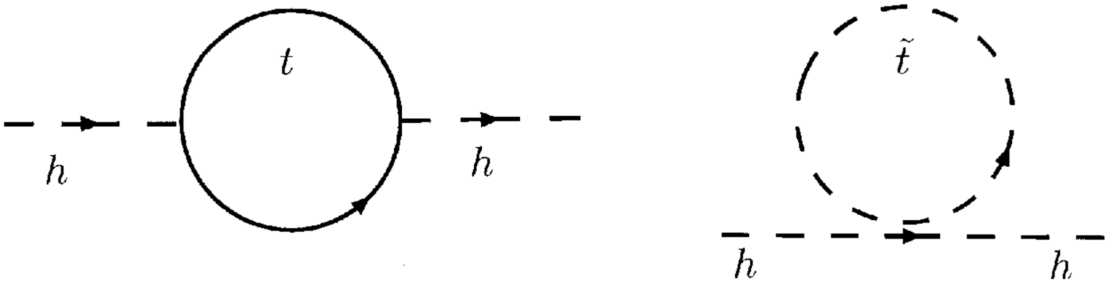

Figure 1.2: The corrections to the Higgs mass calculations due to a Dirac fermion (left) and a scalar S[16]

However, superpartners of the SM particles have not yet been observed experimentally, and hence these particles, if exist, are very massive. In order to avoid the fine-tuning of the Higgs mass, the SUSY particles should have masses not too different from the masses of their SM counterparts, so they should be accessible at the LHC energies. For a detailed description of the theory, please see the reference [17].

In this study, we are working in the framework of R-parity conserving SUSY models, where R-parity is defined as:

$$R = (-1)^{2s+3B+L} \tag{1.4}$$

where, s is the spin quantum number, B is the baryon number and L is the lepton number. The value of R for SM particles is 1 and for SUSY particles is -1. The consequences of R-parity conservation are that SUSY particles are produced in pairs and decay chain of each SUSY particle will end in one Lightest Supersymmetric Particle (LSP), which cannot decay further into any other particle. If the LSP is neutral, stable and weakly interacting, it is a potential candidate for dark matter.

Since the Higgs boson interacts preferably with very massive particles, in the SM, the top quarks contribute maximally to the Higgs mass quantum corrections. Hence, searching for SUSY partners of top quarks at the LHC is of particular interest to stabilize the Higgs boson mass. The current status of these searches at the LHC is summarized in the following section.

1.3 SUSY searches at LHC

As the SUSY theory has a large number of free parameters (e.g. masses of the SUSY particles, their mixing) and many possibilities of underlying assumption, it is very challenging to scan all the theoretical possibilities in experimental analyses. Therefore, the search analyses are designed targeting final state topologies, simplified models of SUSY particle pair production, and simple decay chains generally assuming 100% branching fraction to particular decay modes. The CMS and the ATLAS experiments have dedicated search strategies to look for stop pairs in p-p collision data in a variety of final states.

We are successful in excluding models with stop mass upto 900 GeV, using various analysis strategies and channels. One channel is $\tilde{t}_1 \rightarrow t\tilde{\chi}_1^0$, when the top produced is on-shell i.e. $M_{\tilde{t}_1} \geq M_t + M_{\tilde{\chi}_1^0}$. When the top produced is off-shell and $M_{\tilde{t}_1} < M_t + M_{\tilde{\chi}_1^0}$, then $\tilde{t}_1 \rightarrow bW\tilde{\chi}_1^0$. Even further if $M_{\tilde{t}_1} < M_W + M_b$, then the following channel is valid: $\tilde{t}_1 \rightarrow bff'\tilde{\chi}_1^0$, where *ff'* is a lepton-neutrino pair or a quark-antiquark pair.

The assumed lightest supersymmetric particles for these models i.e. the lighest neutralinos ($\tilde{\chi}_1^0$), which do not interact with the detector gives a signature of missing transverse energy (MET) in the

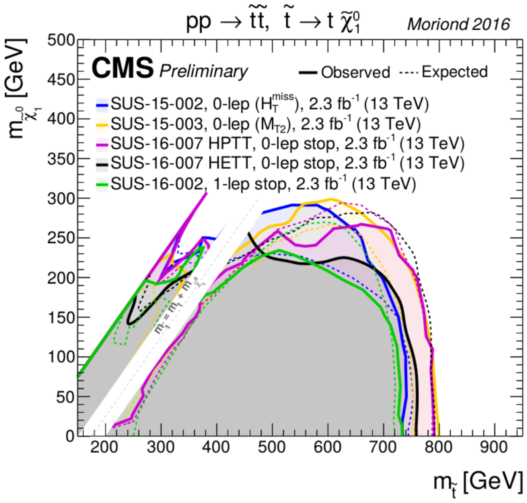

Figure 1.3: Exclusion curves for different analyses including $\tilde{t}$ and $\tilde{\chi}_1^0$ presented in Moriond 2016 analysis (taken from internal CMS sources)

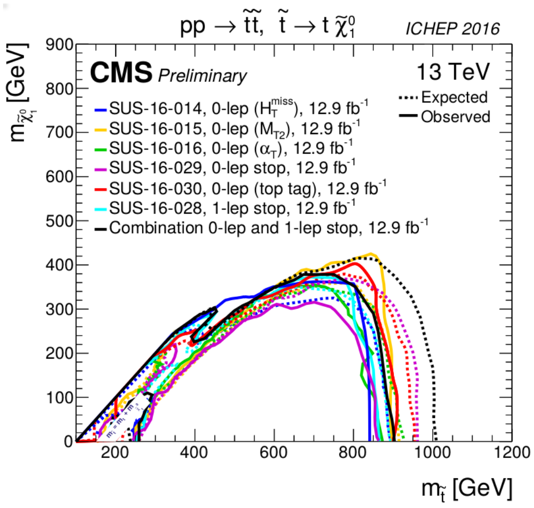

Figure 1.4: Exclusion curves for different analyses including with $\tilde{t}$ and $\tilde{\chi}_1^0$ presented in ICHEP 2016 analysis (taken from internal CMS sources)

detector. Searches based on the measurement of this missing energy have been successful in excluding many of the mass points in the Stop-LSP mass plane. In figure 1.3, it can be noted that it is difficult to probe the models with masses present in the region defined by the line $M_{\tilde{t}_1} \approx M_t + M_{\tilde{\chi}_1^0}$ in the stop-LSP ($M_{\tilde{t}_1}, M_{\tilde{\chi}_1^0}$) mass plane. The higher mass points could be excluded with stronger limits (See figure 1.4) as the events contain a large MET. But for the lower mass stop models in this region, the MET contribution is very small and not a good handle to discriminate against the SM top quark pair production (explained in more details in section 3.2).

Chapter 2

Large Hadron Collider, CMS Detector and Event Reconstruction

2.1 Large Hadron Collider

The Large Hadron Collider is the world's largest particle accelerator built by CERN (European Organization for Nuclear Research). The diameter of this accelerator is 27 km. The LHC is designed to collide proton beams at four collision points and detectors have been constructed to detect the particles produced in the collisions. The collisions using heavy ions like Pb-Pb or Pb-p have also been performed at the LHC. The main purpose of choosing p-p collisions over relatively pure signatures of electron-positron collisions was that the electrons (or positrons) undergo a severe Bremsstrahlung effect in a circular collider losing a lot of energy due to the magnetic field used to bend the colliding particles. The LHC has been designed for the proton-proton centre of mass energy $\sqrt{s} = 14$ GeV and a luminosity $\mathscr{L} = 10^{34} cm^{-2} s^{-1}$. The protons with large energies are collided and two partons i.e. the quarks and gluons in the protons interact (with some probability) with unknown centre of mass energies making it possible to produce particles with a large range of masses.

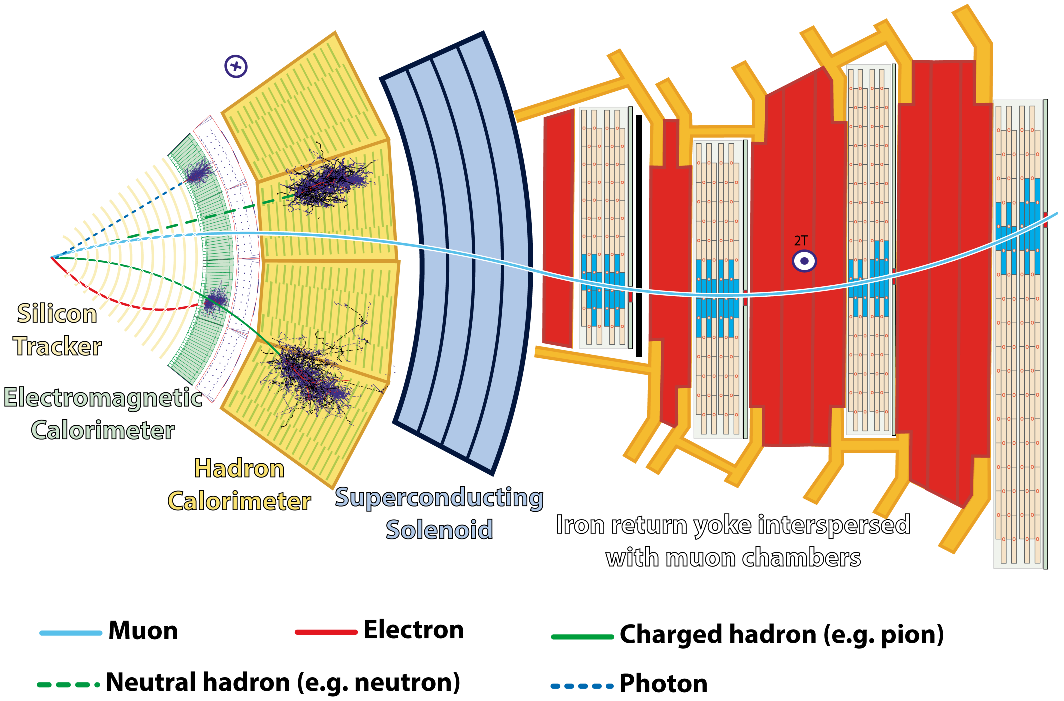

Figure 2.1: The idealized view of the transverse slice of CMS detector from the beam interaction to the muon chambers [19]

2.2 The CMS detector and event reconstruction

The Compact Muon Solenoid (CMS) is one of the two general-purpose detectors at the LHC (another is ATLAS). The purpose of this detector is to search for signatures of new physics, which might be produced in p-p collisions at the LHC. The CMS detector is designed to identify these final state particles as well as to precisely measure their four-momenta and directions. It has a layered structure with different layers optimized to measure specific particles as illustrated in Figure 2.1. The detector is cylindrical in geometry with the beam pipe aligning with the axis of the cylinder.

The geometry of the detector follows the right-handed coordinate system. The interaction point in the beam pipe is considered to be the origin. Z-axis is along the beam axis. The vertical direction is the Y-axis and the X-axis points towards the centre of the LHC ring. The azimuthal angle ϕ is calculated with respect to the X axis in the X-Y plane. Instead of the polar angle, the CMS collaboration uses pseudorapidity, which is defined as

$$\eta = -ln(\tan{(\frac{\theta}{2})}) \tag{2.1}$$

Using these coordinates, the direction of any particle is determined. The component of momentum of a particle in the direction transverse to the beam axis is called its transverse momentum and is denoted by p_T. Along with the p_T, the pseudorapidity η, the azimuthal angle ϕ and reconstructed mass M of the particle provide complete information about the four-momentum of any particle. The particles are identified and reconstructed using the information from all the layers of the detector. Four momenta of all the reconstructed particles along with other properties required for their identification are used in the offline analysis in the ROOT framework (version 5.34 is used) [20] fully supported for high energy data analysis.

2.2.1 Introduction to the detector components

The heavier SM particles like W, Z and H bosons, tau lepton, top quark are unstable and decay into lighter particles like electrons, muons, and neutrinos. The quarks and gluons undergo hadronization. All these final state particles and the hadrons produced in the process deposit their energies as they traverse through the detector material in various components of the detector.

The CMS uses a 3.8 T magnetic field to measure the momenta and charges of the particles produced in the collision. The innermost detectors i.e. tracker and the calorimeters are immersed in the magnetic field. The high bending power before the inner surface of the calorimeter gives strong separation with the energy of the neutral particle deposits for normal incidence.

The CMS tracker is made entirely of silicon. When a charged particle passes through these layers, a small electric signal is created, which then is amplified and detected. Also, the charged particles passing through the tracker bend due to the magnetic field created by the solenoid, hence making it possible to measure both their momenta and charge.

The electromagnetic calorimeter (ECAL) is made of lead tungstate crystals. This lead crystal after adding a bit of oxygen in it becomes highly transparent and scintillates electrons and photons when they pass through it. The photons produced after the scintillation are detected using silicon avalanche photodiodes. Electrons and photons fully deposit their energies via electromagnetic shower. In the barrel (endcaps) region, the crystal length of 23 (22) cm is sufficient to contain almost 98% of the energy of electrons and photons up to 1 TeV. For extra spatial precision, preshower detectors are situated in front of the endcaps. These allow the CMS to distinguish between single high-energy photons (often signs of exciting physics) and the less interesting close pairs of low-energy photons (arising mostly due to decays of π^0 copiously produced in the process of quark and gluon hadronization).

The hadron calorimeter (HCAL) measures the energies of hadrons. It is made up of layers of dense materials (brass and steel) interleaved with the plastic scintillators. The photons produced in the scintillators are directed to hybrid photodiodes using wavelength shifting fibres. The hadrons undergo nuclear interactions with the detector material and result in a cascade of lower-energy particles (called hadronic shower). The energies of these shower particles are deposited in various layers of the detector. The HCAL is very crucial as it ensures that the energetic hadrons are fully contained in the detector, which is very essential for an accurate determination of any imbalance in total momenta of final state particles in the transverse plane.

Unlike electrons, the probability of high energy muons radiating photons and generating electromagnetic showers is extremely small. Hence, these are not stopped inside the calorimeters. The CMS detects muons using three types of detectors: drift tube (DT), cathode strip chamber (CSC) and resistive plate chamber (RPC), which are all gas detectors. The muons knock off the electrons in these gases and the signal is detected. DTs and CSCs are used for the trajectory measurements in the central barrel and endcap regions respectively. RPCs provide a fast signal for muon trigger system and is situated in both the barrel and the endcap regions. The return yokes in this region carry the magnetic field produced by the solenoid in the muon chambers, which helps to track the muons using the similar principle used in the inner tracker. A full description of the CMS detector components is given here [21].

2.2.2 Event Reconstruction at CMS

The CMS uses a particle-flow (PF) algorithm to combine information from the tracker, ECAL, HCAL and muon detectors to provide a list of PF electron, photon, muon, charged and neutral hadron candidates. The PF candidates provide a global interpretation of the particles, which may have been produced in that particular p-p bunch crossing, called an event in the rest of this document.

The CMS uses iterative tracking algorithm for reconstructing tracks using the hits in the tracker, where the hits most consistent with a charged particle are first fitted and removed from the list. The goodness criteria are loosened in the successive iterations, thus maintaining the high efficiency of the identified charged particles as well as maintaining a lower fake rate. The PF algorithm then looks for energy deposits in the calorimeters and performs a geometrical matching with the tracks entering at the surface of the ECAL to form charged PF hadrons. The energy excessive to that consistent with the track momenta is identified as PF neutral hadrons. A full description of the PF algorithm can be found here [22].

Electrons and Muons

Both electrons and photons deposit their energies via electromagnetic cascades, and the technical issues to be solved for tracking and cluster patterns are similar for these. These candidates are selected starting from the blocks that have either an electron seed (a track and an ECAL cluster) or an ECAL topological cluster with $E_T > 10$ GeV. Since the ECAL provides sufficient depth to contain high energy showers, the HCAL energy linked to these should not exceed 10% of the ECAL cluster energy. For low momenta electrons, more weight is given to the tracker measurement. Muons and Electrons should be originated within the 2 mm from the beam axis in the transverse plane. Measurement of photons and high momenta electrons fully rely on calorimeter energy deposits.

The muons are reconstructed by matching the tracks in the inner tracker and the segments/hits in the muon detector. Isolated global muons are identified using a cone of $\Delta R = 0.3$ and the sum p_T of all the additional tracker tracks and E_T of the other hits should not be more than 10% of the muon p_T. This criterion alone is strong enough to identify pure muons.

The mini-isolation is the relative isolation calculated for all the muons and the electrons. In this calculation, the cone size decreases with increasing p_T. The cone size $\Delta R = \sqrt{\Delta\eta^2 + \Delta\phi^2}$, depends on the p_T of the particle.

$$\Delta R = \begin{cases} 0.2, p_T \leq 50GeV \\ \frac{10GeV}{p_T}, 50GeV \leq p_T \leq 200GeV \\ 0.05, p_T \geq 200GeV \end{cases} \tag{2.2}$$

The relative isolation is given by the following formula:

$$\text{Rel Isolation} = \frac{\sum(p_T)_i}{p_{T\,muon}} \tag{2.3}$$

In this analysis, the electrons and the muons are vetoed as this is an all hadronic analysis. The relative isolation should be lesser than 0.1 and 0.2 for electrons and muons, which are being vetoed, respectively. The electron candidates satisfying $p_T > 10$ GeV, $|\eta| < 1.44$, $1.56 < |\eta| < 2.5$ and muon candidates satisfying $p_T > 10$ GeV and $|\eta| < 2.4$ are vetoed.

To reduce the background from the low p_T leptons originating from the W-decays, tracks corresponding to the electrons and the muons are vetoed, if their $p_T < 5$ GeV and $|\eta| < 2.5$, and relative isolation as defined in equation 2.3 within a cone of $\Delta R = 0.3$ is less than 0.2.

Jet Reconstruction

Anti-k_T algorithm [23] is used to reconstruct jets. Using this algorithm all the photons and neutral hadrons, and also all the charged particles, which originate from the primary interaction are reconstructed as jets. Neutral particles from overlapping pp interactions are removed using FASTJET technique. The corrections in energy and momentum of jets are made using the factors obtained from simulations.

CSV b-tagging algorithm

B quarks are identified using the Combined Secondary Vertex algorithm (CSV) [24]. B quarks after being produced hadronize into B hadrons, which are bound states of b quarks. They are heavy, long-lived particles and their decays often contain leptons. Because of its long lifetime, B hadrons decay after traveling some distance from the primary vertex. This distance can be measured using the algorithm and a secondary vertex can be found out using displaced tracks, etc. The jets with $p_T > 30$ GeV and $|\eta| < 2.4$ are considered as the b tagged candidates. The CSV discriminator has a value between 0 and 1. For light flavoured quarks and gluons, this discriminator distribution peaks at a lower value, whereas for b quarks this peaks at a higher value. Three standard working points are used for the b tagging: loose, medium and tight. For this analysis, the jet should pass the medium working point criteria. The misidentification for this is 1.4% and the b-tagging efficiency is 60%.

Missing Transverse Energy (MET)

As the momenta of the colliding particles are in the z-direction (along the beam axis), the momentum in the transverse plane is zero and should remain zero according to the conservation of momentum. But some of the particles like neutrinos, neutralinos, etc. leave the detector without depositing any visible signal, resulting in an imbalance in the total momentum in the transverse plane. Also, some of the jet momenta can be mismeasured which can contribute to this imbalance. Hence, this imbalance in the transverse momenta i.e. the negative of the vector sum of p_T of all the reconstructed particles is defined as missing transverse momentum. The following is the definition for raw MET:

$$\vec{p}_T^{\,miss} = -\sum_{n=1}^{N_{particles}} \vec{p}_{T,n} \tag{2.4}$$

where the sum runs over all the PF particles. Jet energy corrections are also applied to the MET.

The figure 2.2 shows a visual display of a reconstructed CMS event containing two b-tagged jets, two muons and MET, and their directions in the azimuthal plane. This event is a potential $t\bar{t}$ event.

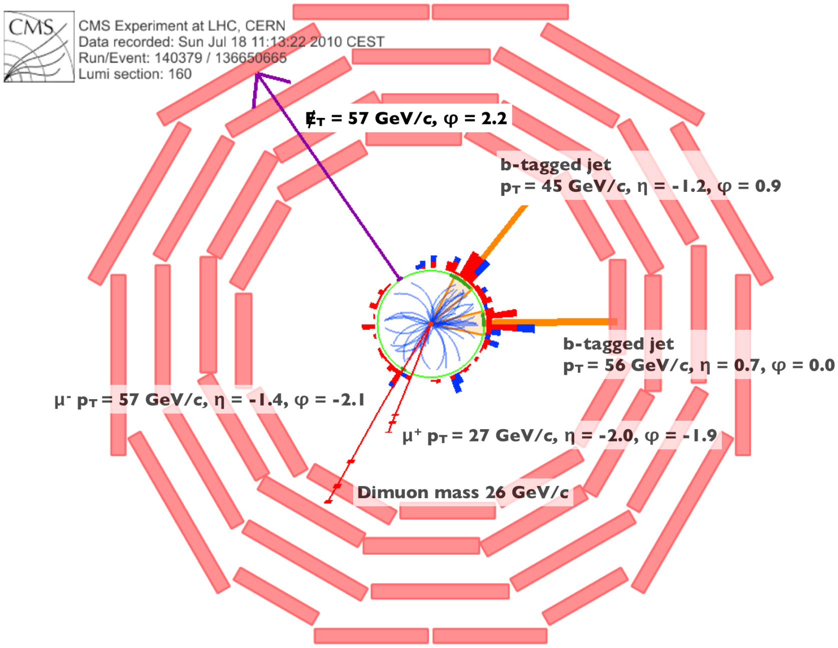

Figure 2.2: Top quark event display, where top is decaying into two muons [25]

2.3 Signal and background Monte Carlo samples

Some of the SM processes can give rise to signatures similar to that of the signal events in the detector. Also, the production cross-sections of these processes are very high compared to those of the signal processes. It becomes crucial to understand the backgrounds faking as signal and reduce their contributions in the signal regions.

The SM processes, which will contribute as backgrounds for the signal SUSY processes to the full hadronic analysis are as follows:

1. $t\bar{t}$ production (Dilepton and Single Lepton)
2. QCD Multijet
3. W (l, ν) + Jets
4. Z (ν, ν) + Jets

MADGRAPH5 [26] generator is used to simulate these SM samples, Pythia8.1 [27] and underlying-event tune CUETP8M1 [28] are used for the parton showering and the hadronization. The cross sections are calculated using next-to-next-to-leading-order (NNLO) diagrams except for QCD samples (Leading order-LO).

The Standard model processes, which contribute to the dilepton analysis are as follows:

1. $t\bar{t}$ production (Dilepton and Single Lepton)

2. Drell Yan

3. Single Top (tW channel)

4. Multiboson (WW, WWZ, ZZ, ZZZ, WZ, WZZ etc)

5. TTZ ($ll, \nu\nu$ or q$\bar{q}$)

6. TTW + Jets

Most of these backgrounds have been produced using MADGRAPH5 generator, with pythia8 and underlying-event tune CUETP8M1. Single-top events produced in the tW channel are generated with Powheg v1.0, and rare SM processes such as TTZ and TTW are produced using MADGRAPH_AMC@NLO program. Next-to-leading-order (NLO) NNPDF3.0 [29] are used in both these cases.

The NNPDF3.0 PDFs [29] are used for the stop pair production. The signal model points used are as follows: (M_{Stop},M_{LSP}) $\equiv$ (175,1), (200,25), (225,50), (250,75), (275,100), (300,125). All these model points lie in the top corridor region. The signal points (400,25), (425,50), (450,75), (475,100), (500,125) are also used for the analysis, to check the usefulness of the analysis for high mass samples. The events are produced at leading order but cross-sections including higher order are available and are used to normalize the event yields to target luminosity scenarios.

The generated events are processed through a GEANT4 based detailed simulation of the CMS detector[30] to include the effect of the detector response. This includes the simulation of the detector readout electronics (this step is also called as digitization). This information is then used for reconstruction of all the events. These reconstructed events are stored in reduced format in the form of Ntuples (ROOT) and then used for the analysis purpose. The simulated event samples are used to understand the signal and the backgrounds and develop a search analysis strategy using both zero lepton and dilepton events as these closely model what we would expect in the data.

Chapter 3

Understanding $\tilde{t}\tilde{t}^*$ signature in the top corridor region

The purpose of this study is to identify pp collision events, which might contain a pair of top squarks (stop), where each of the stops decays to a SM top quark and a neutralino, $\tilde{t} \rightarrow t + \tilde{\chi}_1^0$ (See Figure 3.1). In this model, the $\tilde{\chi}_1^0$ is assumed to be weakly interacting, stable lightest SUSY particle (LSP). As a result, the $\tilde{\chi}_1^0$ escapes the detector without leaving any visible signature, just like the SM neutrinos and therefore contribute to the MET (Missing Transverse Energy).

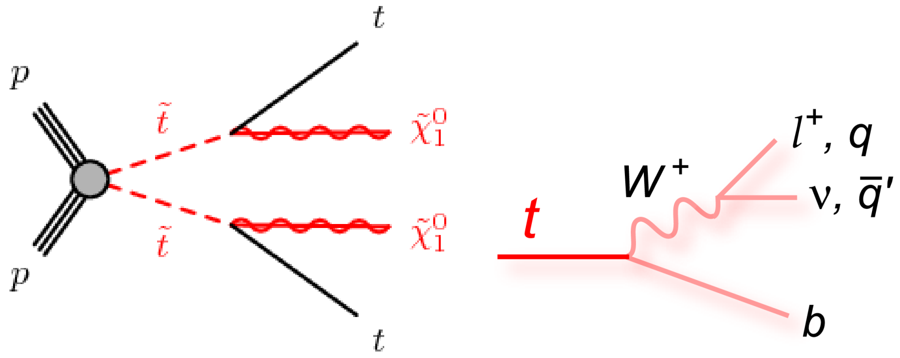

Figure 3.1: Signal Topology: $\tilde{t}$ - stop, $\tilde{\chi}_1^0$ - neutralino. (References:-[33] and [31])

In the SM, the top quark decays to a b quark and a W boson with almost 100% branching fraction

[32]. The W boson decays into quark pairs and lepton pairs with a branching fraction of approximately 68% and 32% respectively [32]. The table 3.1 lists the branching fractions for all the decay modes for events containing two W bosons. A $\tilde{t}\tilde{t}^*$ event sample will result into a zero lepton or all hadronic final state with 45.44% branching ratio and dilepton (ee, $e\mu$,$\mu\mu$) final state with 4.56% branching ratio. Each of these final states are accompanied by b-quark jets and MET due to two LSPs. In addition, each of the lepton is accompanied by the respective neutrino, adding contribution to the MET.

Branching ratios in % for two Ws	$e-\nu_e$	$\mu-\nu_\mu$	$\tau-\nu_\tau$	$q-\bar{q}$
$e-\nu_e$	1.15	1.14	1.22	7.22
$\mu-\nu_\mu$	1.14	1.13	1.21	7.17
$\tau-\nu_\tau$	1.22	1.21	1.30	7.67
$q-\bar{q}$	7.22	7.17	7.67	45.44

Table 3.1: Branching fractions for all the decay modes of a pair of W bosons.

For a new physics search analysis, it is desirable to have maximum signal acceptance i.e. a set of event selection criteria, which accepts maximum signal events. However, many SM processes can give rise to similar final states and owing to their large production cross-section, can hide a potential signal. The level of backgrounds is process dependent. All hadronic decay modes of top or stop pairs have higher branching fractions, hence large signal efficiency. Also, in full hadronic channel, it is possible to fully reconstruct the top kinematics and use top quark as a probe to new physics. However, the QCD multijet events can fake as signal events and these backgrounds are challenging to measure. On the other hand, leptons are well reconstructed objects. The dominant backgrounds are electroweak in nature, which are well understood theoretically and experimentally.

In this study, an analysis strategy is developed to search for $\tilde{t}\tilde{t}^*$ production in all hadronic (no leptons) and dileptonic (two leptons - ee, $e\mu$,$\mu\mu$), in the phase space where difference in masses of the $\tilde{t}$ and $\tilde{\chi}_1^0$ is almost equal to the mass of the top quark. In the following section, kinematics of final state products is investigated to understand the differences with respect to the SM $t\bar{t}$ production which has a similar signature as that of the SUSY topology considered in this thesis.

3.1 Kinematics of top quarks and MET

In the $\tilde{t}\tilde{t}^*$ scenarios with $\tilde{t} \rightarrow t + \tilde{\chi}_1^0$, every event has two top quarks and MET due to the two LSPs. It closely resembles the SM $t\bar{t}$ production, which has much higher cross-section even for similar masses of top and stop. The following distributions are made using generator level information and are normalized to the unit area, i.e. the purpose is to show only shape comparisons.

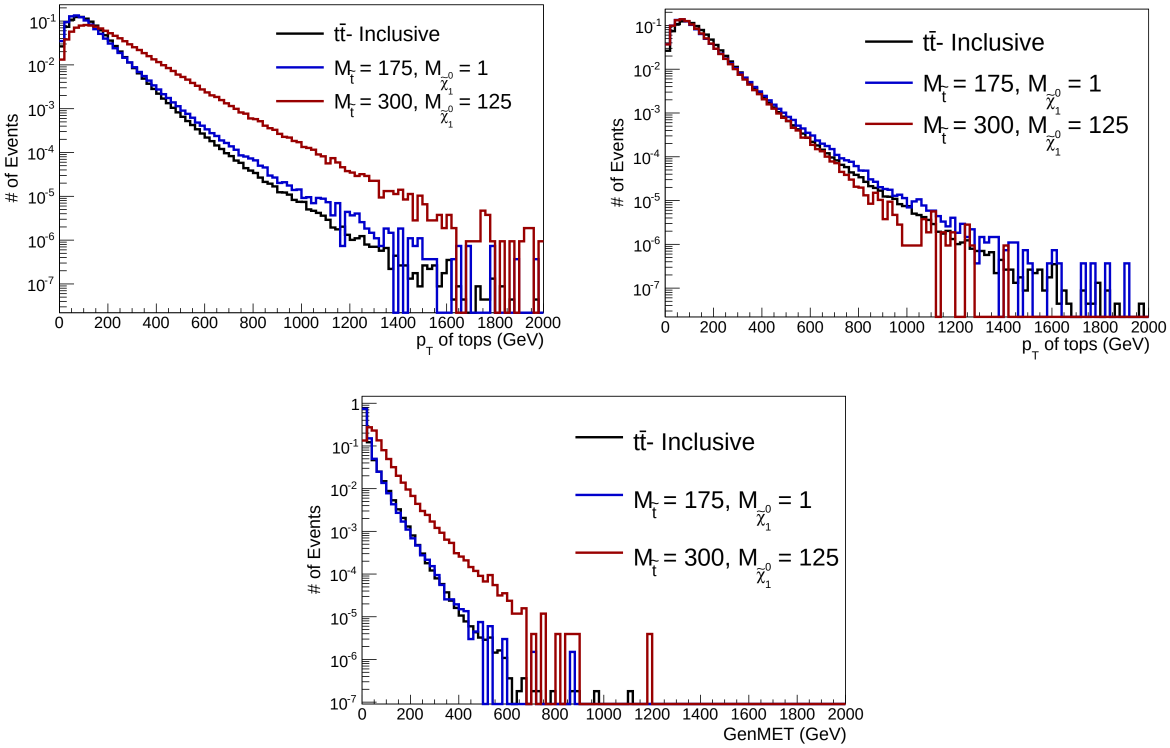

Figure 3.2: (top left) p_T Distribution of tops and stops produced directly from p-p collision in $t\bar{t}$ and $\tilde{t}\tilde{t}^*$ events, (top right) p_T of tops in $t\bar{t}$ and $\tilde{t}\tilde{t}$ events, and (bottom) GenMET Distribution for $t\bar{t}$ and $\tilde{t}\tilde{t}$ events

All the signal model points are in the top corridor region, which is explained in the next section (section 3.2). In the top left plot of figure 3.2, the distributions of p_T of top quarks in $t\bar{t}$ events are compared with the p_T distributions of stops of different masses (175 GeV and 300 GeV) in $\tilde{t}\tilde{t}^*$ events. As expected, the average p_T is observed to be higher for the stops with higher masses. However, the distributions of top p_T in $t\bar{t}$ events and the stop p_T in the events with $M_{\tilde{t}} = 175$ GeV are similar. As shown in top right figure, the various distributions of top p_T for different stop masses are almost identical to those observed in the SM $t\bar{t}$ events. The bottom figure shows comparison of the GenMET (MET calculated using the particles with decay length $(c_\tau) \approx 1$ cm in Pythia, τ is particle lifetime in the rest frame) distributions and clearly the GenMET shapes are same in the case of $t\bar{t}$ and $M_{\tilde{t}} = 175$ GeV events. The current MET based analysis uses a tighter MET requirement, which rejects these models with stop mass closer to the top mass making it difficult to probe this phase space. For higher stop masses, the MET spectra is harder and can serve as a search variable.

3.2 Relativistic kinematics of the top corridor and its implications

In the context of the topology being used, $M_{\tilde{t}}$ and $M_{\tilde{\chi}_1^0}$ are free quantities in the theory and these have to be experimentally determined. Therefore, all the possibilities have to be considered. This particular study targets the signal phase space where $M_{\tilde{t}} \approx M_t + M_{\tilde{\chi}_1^0}$. This compressed region is called the "top corridor" (See figure 1.3). Currently all hadronic MET based stop searches put strong exclusion limits on high mass stop models, but these limits are weaker for lower masses or models particularly in the top corridor region. Most of these searches rely on high MET selection and it is observed in the previous section that the MET shape is similar for signal and background events for low mass stops. In this section, we try to elaborate on these features.

As the models in the top corridor satisfy

$$M_{\tilde{t}} \approx M_t + M_{\tilde{\chi}_1^0} \tag{3.1}$$

the products of stop (top and neutralino) are produced at rest in the frame of stop.

Six signal model points, which have not been excluded are being used for this analysis: where $(M_{Stop}, M_{LSP}) \equiv (175,0), (200,25), (225,50), (250,75), (275,100), (300,125)$. The plot of average p_T of stops versus M_{Stop} (see figure 3.2) shows that:

$$p_{T_{Stop}} \approx M_{Stop} * 0.6 \tag{3.2}$$

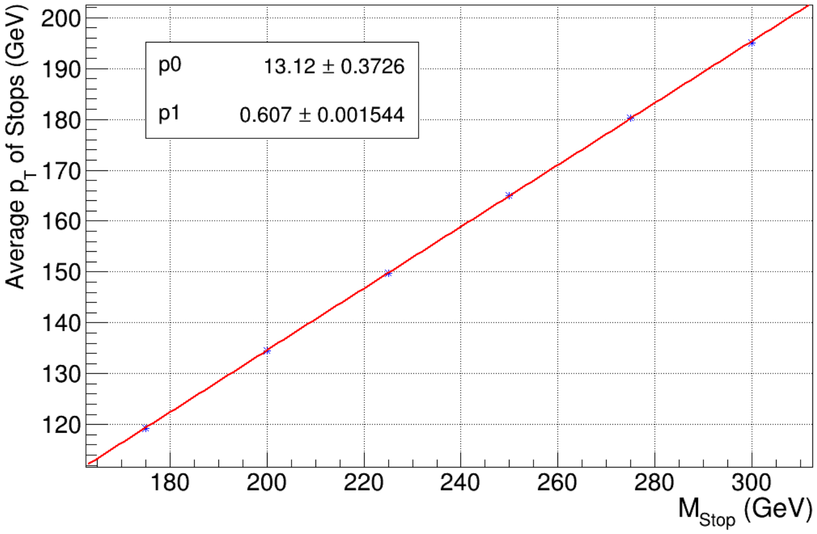

Figure 3.3: Average p_T of stops versus M_{Stop}. Here p0 and p1 are the constants in the equation y=p1*x + p0, where y axis is the average p_T of stops and x-axis is the mass of stop

Here, in this case,

$\beta\gamma = 0.6$, $\gamma = 1.17$.

Consider that the transverse momentum and the energy of LSP in the lab frame are denoted by P and E and in the stop frame are denoted by P' and E'.

If we write the transformation of momentum vector of LSP from the stop frame to the lab frame, we obtain the following:

$$\begin{bmatrix} E \\ P \end{bmatrix} = \begin{bmatrix} \gamma & \beta\gamma \\ \beta\gamma & \gamma \end{bmatrix} \begin{bmatrix} E' \\ P' \end{bmatrix} \tag{3.3}$$

Substituting the values of γ and $\beta\gamma$:

$$\begin{bmatrix} E \\ P \end{bmatrix} = \begin{bmatrix} 1.17 & 0.6 \\ 0.6 & 1.17 \end{bmatrix} \begin{bmatrix} \sqrt{{M_{LSP}}^2 + P'^2} \\ P' \end{bmatrix} \tag{3.4}$$

In the top corridor, P'=0 as top and neutralino are produced at rest in the frame of stop. Therefore, we get that

$$P'_{LSP} \approx 0.6 * M_{LSP} \tag{3.5}$$

i.e. $P'_{LSP} \propto M_{LSP}$. So, in the top corridor, if $M_{LSP} \approx 0$, then $p_{T\,LSP} \approx 0$ i.e. the contribution of LSP momentum to the MET is zero. These events are very similar to the events with top pair production. It becomes difficult to differentiate between these events. New analysis strategies are explored to achieve this distinction between the background and the signal events.

3.2.1 ISR Tagging method

Initial State Radiation is the radiation coming from the initial state of the partons produced. So, selecting a very high momentum ISR jet can boost the remaining $\tilde{t}\tilde{t}^*$ system conserving the momentum of the colliding partons (See figure 3.4). This aligns the neutralinos in the event almost in the same direction, which increases the vector sum of their p_Ts. This contributes to the MET significantly and a higher MET threshold can be applied in the event selection.

From the relativistic calculations, it is found that

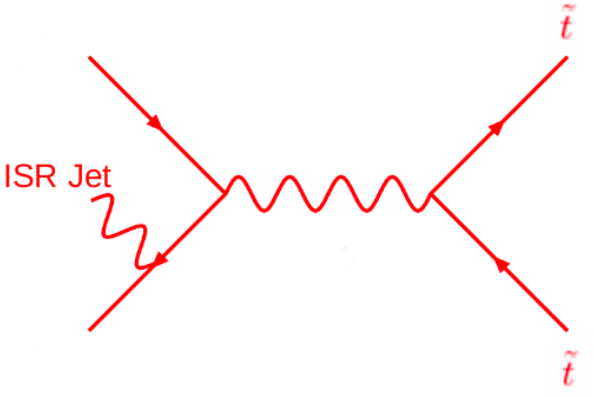

Figure 3.4: Initial State Radiation

$p_{T_{\tilde{t}}} \approx M_{\tilde{t}} * 0.6$ and $p_{T_{\tilde{\chi}_1^0}} \approx M_{\tilde{\chi}_1^0} * 0.6$.

Which gives:
$$\frac{p_{T_{\tilde{t}}}}{M_{\tilde{t}}} = \frac{p_{T_{\tilde{\chi}_1^0}}}{M_{\tilde{\chi}_1^0}}. \tag{3.6}$$

This can be rearranged to give:
$$p_{T_{\tilde{\chi}_1^0}} = \frac{M_{\tilde{\chi}_1^0}}{M_{\tilde{t}}} * p_{T_{\tilde{t}}} \tag{3.7}$$

Here, $\frac{M_{\tilde{\chi}_1^0}}{M_{\tilde{t}}}$ is constant for a particular model of stop. To probe this constant, we have to have $p_{T_{\tilde{t}}}$, which is not experimentally determined. So, we use ISR jet p_T as a proxy to this. This can be done because of the following equation:
$$p_T^{ISR} = -(p_{T_{\tilde{t}}} + p_{T_{\tilde{t}*}}) \tag{3.8}$$

Considering identical momenta of stops and LSP, we can write for a given signal model:

$$p_{T_{\tilde{\chi}_1^0}} \propto MET, p_{T_{\tilde{t}}} \propto p_T^{ISR} \tag{3.9}$$

So, we can write the constant $\frac{M_{\tilde{\chi}_1^0}}{M_{\tilde{t}}}$ as R_M [36] and it can be written using kinematic variables as follows:

$$R_M = \frac{p_T^{miss}}{p_T^{ISR}} \approx \frac{M_{\tilde{\chi}_1^0}}{M_{\tilde{t}}} \tag{3.10}$$

For a given stop-LSP model, we expect to see a peak-like feature in the distribution of this variable. We investigated this kinematic variable for low mass stop analysis in the top corridor.

3.3 Spin Correlation Method

The higher MET threshold in MET based searches makes it difficult to search for the signal models with low LSP masses. This is because the p_T of the low mass LSPs does not contribute much to the MET. This can be seen in equation 3.5. The $t\bar{t}$ and the $\tilde{t}\tilde{t}^*$ have similar signatures in case of lower LSP models as explained in section 3.2. So, a method which depends upon the fermionic and bosonic natures of $t\bar{t}$ and $\tilde{t}\tilde{t}^*$ events, respectively, can be used to achieve the distinction between these two processes.

The SM predicts the transfer of spin information of $t\bar{t}$ to the decay products, which has been observed at the LHC [34] [35]. But the scalar stop does not have spin and the spin correlation between the decay products of the stop is not expected. In SUSY, the polarization of stops can vary. The samples used in this analysis are unpolarized i.e. mixture of stops of both the polarizations (right-handed and left-handed). Like helicity gluon fusion is the dominant channel for top pair production. As the two gluons have the same helicity, the tops produced have their spins anti-parallel with each other. In case of less boosted top pair production, because of the angular momentum conservation and the V-A structure of the charged current weak interaction the direction of the two leptons produced is the same. The figure 3.5 shows the directions of all the decay products produced.

Considering events with all the values of $M_{t\bar{t}}$, the distributions of $\Delta\phi(l_1,l_2)$ (figure 3.7) (where l_1 and l_2 are the leptons in the dilepton events) show a small difference between $t\bar{t}$ and $\tilde{t}\tilde{t}^*$ events (these distributions are made using the parton level leptons). Figure 3.6 shows the $M_{t\bar{t}}$ distributions for $t\bar{t}$ events and signal events with $M_{\tilde{t}} = 175$ GeV and 300 GeV. These events were further divided in two different regions of $M_{t\bar{t}}$ i.e. $M_{t\bar{t}} \leqslant 450$ GeV and $M_{t\bar{t}} > 450$ GeV. The p_T distributions for two tops were observed for the events in these two regions (See figures 3.8 and 3.9). The events with $M_{t\bar{t}} \leqslant 450$ GeV contain tops which are lesser boosted and the events with $M_{t\bar{t}} > 450$ GeV contain tops with larger boost. Figure 3.10 shows that the $\Delta\phi(l_1,l_2)$ distribution for $t\bar{t}$ events for the tops with $M_{t\bar{t}} \leqslant 450$ GeV peaks at a lower value of $\Delta\phi$ (around 0) and that for $\tilde{t}\tilde{t}^*$ peaks at a value closer to π. In case of the higher invariant mass of the $t\bar{t}$ system, the two tops are boosted and are back to back. So, the leptons produced have an opening angle almost equal to 180^0, because of which the $\Delta\phi(l_1,l_2)$ distribution peaks at a higher value (near π) for both $t\bar{t}$ and $\tilde{t}\tilde{t}^*$ events (see figure 3.11). All the distributions of $\Delta\phi(l_1,l_2)$, $M_{t\bar{t}}$ and p_T of tops have been normalised to unit area, so that only the shape comparisons are shown here.

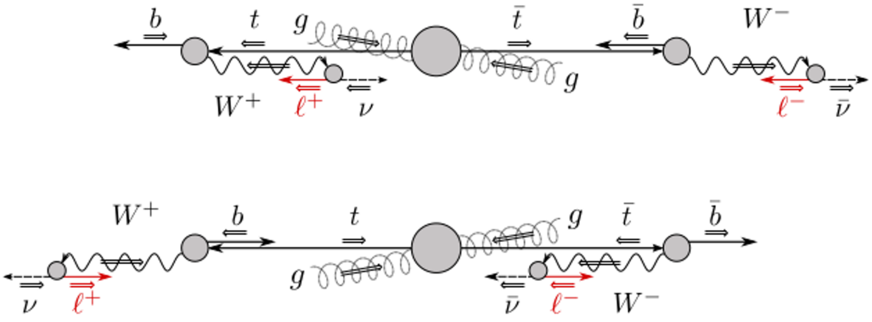

Figure 3.5: Decay products of tops and their directions of flight due to the spin correlation between the products [33]

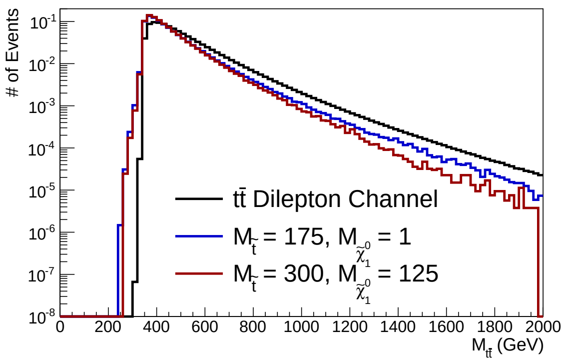

Figure 3.6: $M_{t\bar{t}}$ Distributions

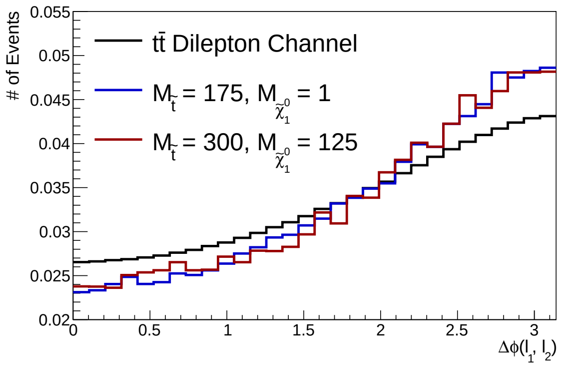

Figure 3.7: $\Delta\phi(l_1, l_2)$

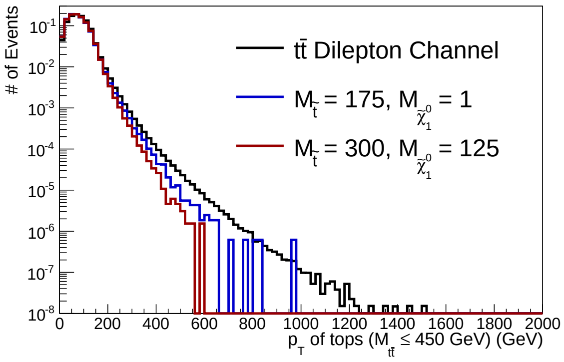

Figure 3.8: Transverse momenta of tops produced for $M_{t\bar{t}} \leqslant 450$ GeV

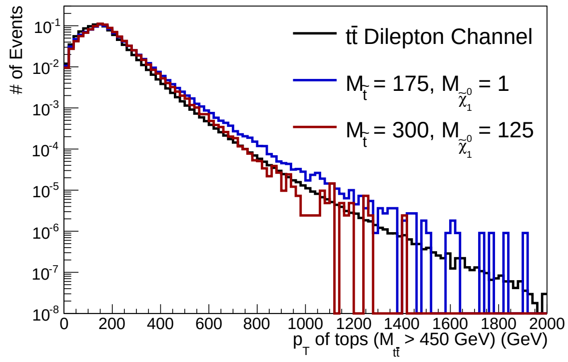

Figure 3.9: Transverse momenta of tops produced for $M_{t\bar{t}} > 450$ GeV

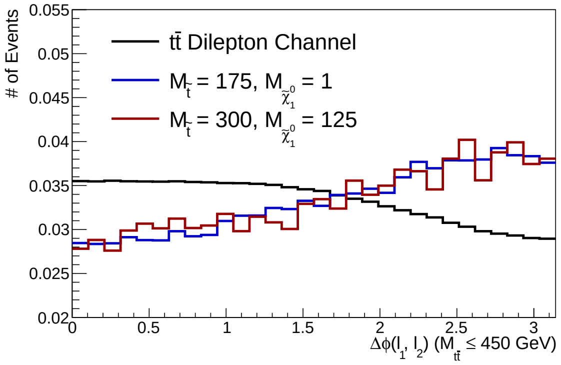

Figure 3.10: $\Delta\phi(l_1, l_2)$ for $M_{t\bar{t}} < 450$ GeV

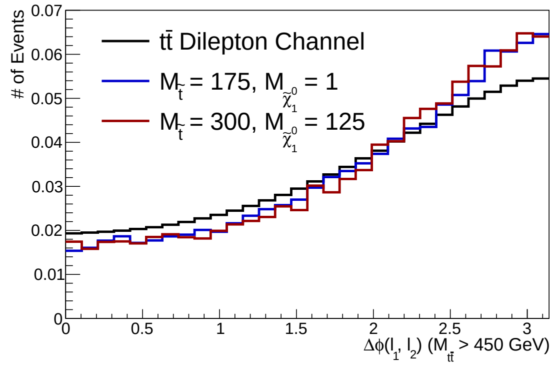

Figure 3.11: $\Delta\phi(l_1, l_2)$ for $M_{t\bar{t}} > 450$ GeV

Chapter 4

Stop search in all-hadronic final state using ISR tagging

4.1 Baseline Selection

The CMS collaboration has dedicated searches to look for stop pairs in fully hadronic final states, and these analyses mostly rely on MET as a discriminating tool. In this study, we propose an alternative strategy, which uses the events with a high p_T ISR tagged jet. However, we follow the basic object selection criteria described in the CMS publication [18]. Since we are aiming for a full hadronic analysis, events containing a number of jets in a final state accompanied by MET are to be studied as backgrounds. In addition, detector noise, non-functioning detector channels, and reconstruction failures can cause fake MET signature. We apply MET filters recommended by the collaboration to remove such events. Figure 4.1 shows MET distributions for all the processes before applying any selection and figure 4.2 shows these after applying MET filters. As expected, these filters do not affect the distributions predicted by the Monte Carlo simulations.

In $t\bar{t}$ and W+ jets events, the leptonic channel contributes to the MET as the final states have neutrinos. Rejecting the events with leptons removes most of these background events. An event is vetoed if it contains a muon (electron) candidate with $p_T > 10$ GeV and $|\eta| < 2.4$ ($|\eta| < 2.5$) and relative isolation less than 0.2 (0.1) as explained in equation 2.3. The MET distributions after applying muon and electron vetoes are shown in figures 4.3 and 4.4.

Due to the kinematic acceptances used in the lepton reconstruction some of the $t\bar{t}$ and W+ jets events are not vetoed. Also, the backgrounds due to the tau leptons decaying hadronically are not vetoed by the lepton veto criteria. To reduce these backgrounds further, an isolated track veto, as explained in section 2.2.2, is used. The isolated tracks consistent to be originating from muons and electrons should have $p_T > 5$ GeV, $|\eta| < 2.5$ and relative isolation < 0.2. Those originating from charged hadrons should have $p_T > 10$ GeV, $|\eta| < 2.5$ and relative isolation < 0.1. To ensure that the isolated track candidates potentially coming from W decays are rejected, the isolated track candidate should satisfy the following criterion:
$M_T(tk, p_T^{miss}) = \sqrt{2p^{tk}p_T^{miss}(1 - cos\Delta\phi)} < 100$ GeV. The MET distributions after applying the isolated track veto are shown in the figure 4.5.

The jets for the purpose of the analysis have been selected according to the criteria mentioned in the CMS publication[18]: $p_T \geqslant 30$ GeV, $|\eta| < 2.4$. In addition to the leading jet, the remaining stop system should contain at least 5 jets, the criterion which has been tightened from 4 jets used in the CMS study[18], to reduce the QCD background (explained at the end of this section). In the stop system, the first two leading jets should have $p_T > 100$ GeV and the next two jets should have $p_T > 50$ GeV, which has been changed from $p_T > 50$ GeV and $p_T > 30$ GeV respectively mentioned in [18]. There should be at least one b-tagged jet in the stop system. A jet is considered to be a b-tagged jet only if it passes the medium working point criteria in "Combined Secondary Vertex" method explained in section 2.2.2. The figures 4.6 and 4.7 show MET distributions after the number of jets and the number of b-tagged jets criteria. This further reduces W+Jets and Z+Jets backgrounds as they do not produce b quarks.

Initially, a cut of 50 GeV is applied on MET. This is to have some minimum requirement on the MET for the calculations of $\Delta\phi$ between MET and other jets, for defining ISR jet as well as angular cuts to reject QCD events with jet mismeasurements.

It is important to make sure that the leading jet of the events selected is an ISR jet. This jet is in addition to the minimum 5 jets comprising the stop system as explained above. After studying the signal acceptance for ISR jet p_T thresholds in the range 450-800 GeV, ISR jet $p_T > 700$ GeV was selected for further development of the analysis strategy. The figure 4.8 shows the distributions of p_T of ISR jets before selecting the ISR jet. Also, this ISR jet should not be a loose b-tagged jet as we do not expect it to originate from top quark decay. As the ISR jet is highly boosted, the stop system and the ISR jet should be back to back. This means the MET resulting from the two LSPs should be opposite to the ISR jet, and the following criterion is applied to select such events: $|\Delta\phi(MET, ISR) - \pi| < 0.2$. The figure 4.9 shows the distributions of $\Delta\phi$ between the ISR jet and MET in signal and backgrounds events. This criterion selects almost all the events in the last two bins rejecting a majority of background events, while retaining modest signal acceptance. Before selecting any ISR jet, the MET distributions for all signal events look similar except the cross section effects (figure 4.10). But after selecting a hard ISR jet, the entire stop system is back to back with the ISR jet and is boosted in the opposite direction. This aligns both the neutralinos almost in one direction so that their vector sum and hence the MET contribution is increased. Also, their momenta highly depend upon the masses of the neutralinos according to Equation 3.5. As the contribution of the neutralino p_T to the MET is significant in stop events, for higher neutralino masses, the MET is higher, as observed in figure 4.11. Similar trends are also observed in the case of R_M distributions, which are shown in figures 4.12 and 4.13. The distributions peak at different values according to the value of $\frac{M_{\tilde{\chi}_1^0}}{M_{\tilde{t}}}$ corresponding to the particular signal model.

To reduce the MET due to mismeasurement of jets, mainly in QCD events, a criterion $\Delta\phi(MET, jet_{(1,2)}) > 0.3$ is applied, where $jet_{(1,2)}$ are the leading two jets which are components of the stop system and not the ISR jet (a criterion has already been applied for that). The events surviving after this selection were divided into two categories based on different selections applied. These two selections are $MET > 200GeV$ and $R_M > 0.3$. For the ISR jet having $p_T \approx 700$ GeV and $MET \approx 200$ GeV, the $R_M (= \frac{p_T^{miss}}{p_T^{ISR}})$ will have value around 0.3. That is why these two selections are comparable.

In order to further reduce the QCD background contribution, the jet multiplicity distributions are revisited and are shown in figure 4.14. As clearly visible, the QCD events dominate in the first bin (Njets=5) of jet multiplicity distributions. Tightening the threshold on this variable the improvement in the signal to background ratio is seen. Therefore, the Njets$\geqslant$ 6 is used for the final selection. After this selection, the distributions of MET in figures 4.15 and 4.16, and those of R_M in figures 4.17 and 4.18 show that the QCD events are concentrated in the bins having lower values of R_M or MET. This concentration is more in case of R_M distributions than in case of MET distributions. So, tightening the requirement on R_M might help in reducing QCD events to a great extent in the final analysis. This can be seen in case of both the selections i.e. MET >200 GeV and $R_M > 0.3$.

The cutflow after applying subsequent selection criteria for different optimizations are provided in table 4.1. This shows the number of events survived after every selection.

Selection	**QCD**	$t\bar{t}$	**W + Jets**	**Z + Jets**	**Total Bkg**	**(175,1)**	**(200, 25)**	**(225, 50)**	**(250, 75)**	**(275, 100)**	**(300, 125)**
No cut	1099362379	13342550	55714708	13800284	1182219922	3642480	1935253	1091454	647846	399693	255484
MET Filters	1099327290	13342496	55714482	13800257	1182184527	3642469	1935245	1091448	647843	399691	255480
Muon Veto	1098152301	8569289	41642746	13787390	1162151727	2909083	1543920	868912	515416	317522	202910
Electron Veto	1091947754	4810214	29026232	13747770	1139531972	2329923	1234388	693449	411359	252796	161575
Iso Track Veto	1035775725	3048753	22334035	13144493	1074303007	1812033	959684	540637	321137	197777	126511
NoJets$\geqslant$5	219443476	640695	269896	108663	220462732	708829	396322	234569	144147	92025	60467
No of b-tagged jets$\geq$ 1	39062851	467506	42401	18457	39591217	516698	290845	173409	107059	68557	45162
MET$>$50GeV	9604773	335116	28842	15353	9984086	144467	114920	87419	62447	44197	31027
ISR jet (leading jet) pT$>$700GeV and not a loose b-tagged jet	114054	855	311	180	115401	500	495	399	313	224	194
$\lvert\Delta\Phi(ISR,MET)-\pi\rvert <$**0.2**	39653	299	77	39	40069	171	245	247	184	143	125
Tightening p_T **requirement**	18811	182	35	16	19046	112	193	181	137	112	89
MET$>$200GeV	1509	115	16	11	1652	42	68	126	123	104	86
OR											
$R_M >$**0.3**	499	84	12	9	606	24	32	86	97	93	82
(MET$>$200GeV) $\Delta\phi(MET, jet_{1,2}) >$**0.3**	179	30	4	4	219	8	14	33	43	39	36
OR											
($R_M >$**0.3)** $\Delta\phi(MET, jet_{1,2}) >$**0.3**	44	23	3	4	75	2	7	23	33	37	35
(MET$>$200GeV) $NoJets \geqslant 6$	130	26	2	3	163	5	9	25	39	35	31
OR											
($R_M >$**0.3)** $NoJets \geqslant 6$	27	20	1	2	52	2	5	17	30	33	30

Table 4.1: Cutflow table for all the selections applied in the full hadronic analysis

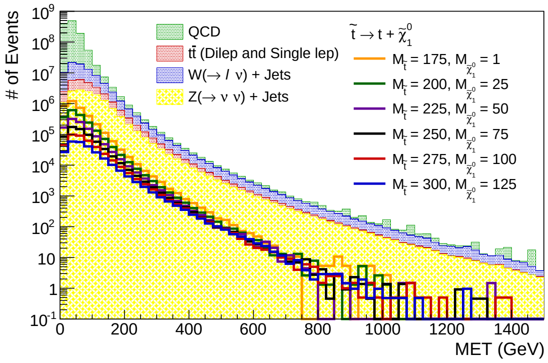

Figure 4.1: MET distributions: Before applying any selection

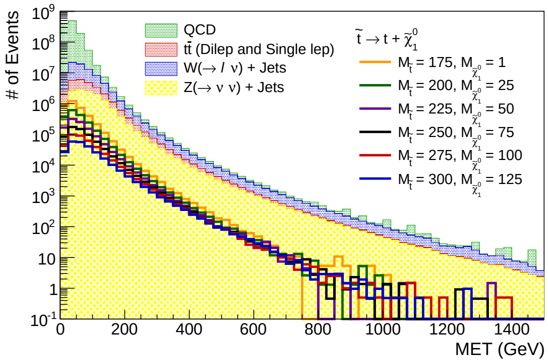

Figure 4.2: MET distributions: After applying MET Noise Filters

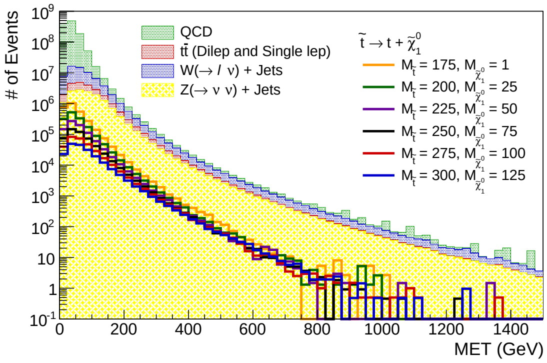

Figure 4.3: MET distributions: After applying Muon Veto

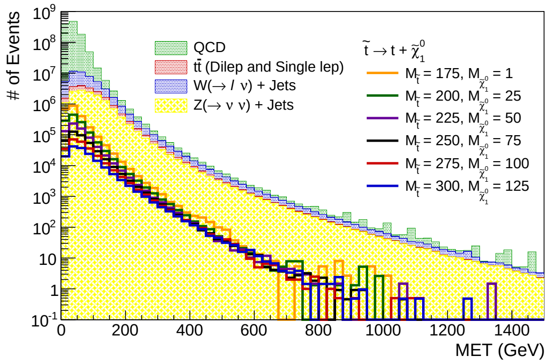

Figure 4.4: MET distributions: After applying Electron Veto

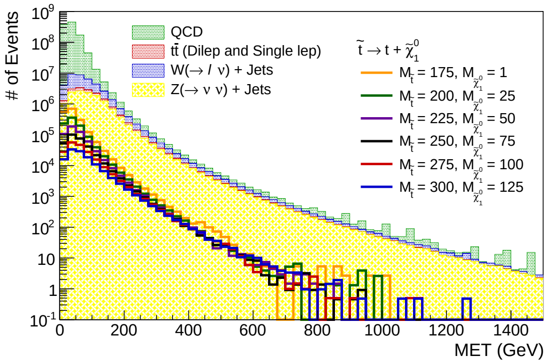

Figure 4.5: MET distributions: After applying isolated tracks veto

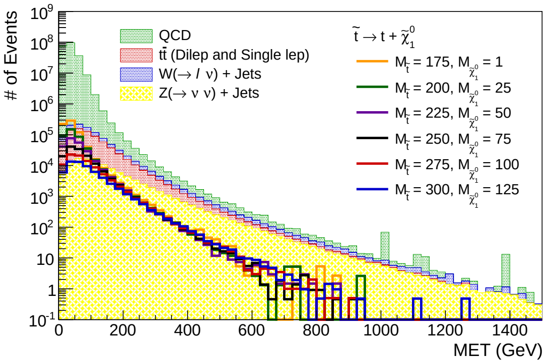

Figure 4.6: MET distributions: After applying number of jets selection

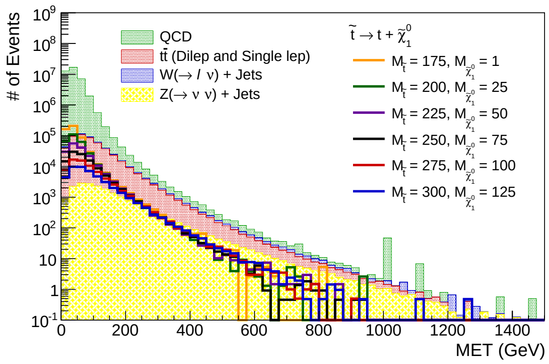

Figure 4.7: MET Distributions: After applying a number of b-tagged jet criterion

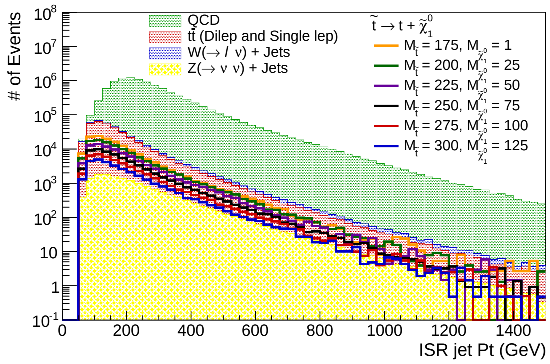

Figure 4.8: ISR jet pT distributions: After applying the initial MET $>$ 50 GeV cut. All the events which have ISR pT greater than 700 GeV have been selected.

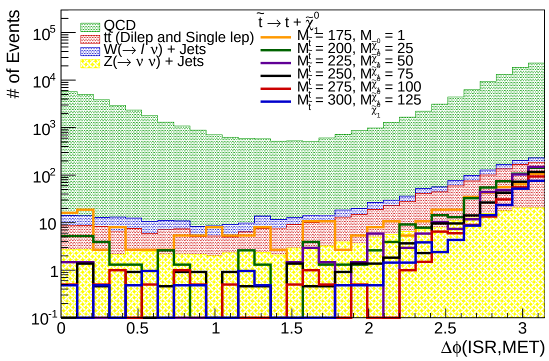

Figure 4.9: Distributions of $\Delta\phi$ between the ISR jet and MET: After applying the ISR p_T criterion.

4.2 Results and discussion for the full hadronic analysis

To check the exclusion potential for a given stop model, the upper limit on the value of the parameter r is calculated with 95% confidence level, where r is defined as

$$r = \frac{number\ of\ signal\ events\ observed}{number\ of\ expected\ signal\ events} \tag{4.1}$$

The total number of events observed can be written as: # of signal events $= \mathscr{L} * \sigma * R$, where

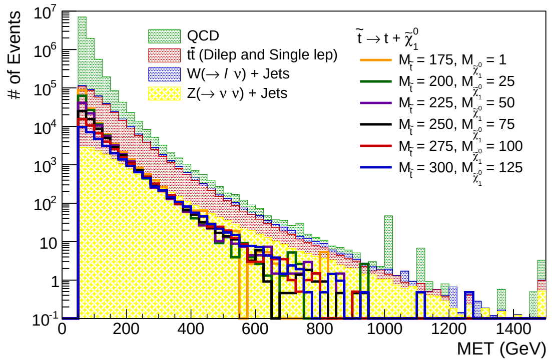

Figure 4.10: MET distributions: After applying the initial MET $>$ 50 GeV selection (Just before selecting the ISR jet)

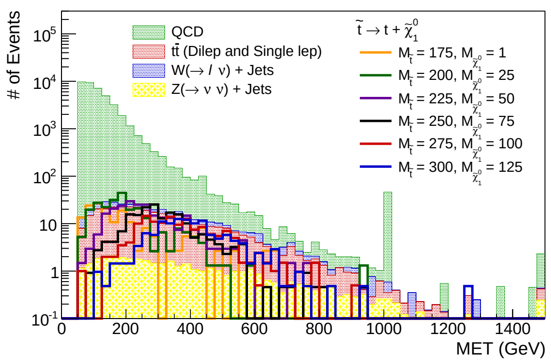

Figure 4.11: MET distributions: After selecting the ISR jet. The peaks are clearly distinguishable for every signal point

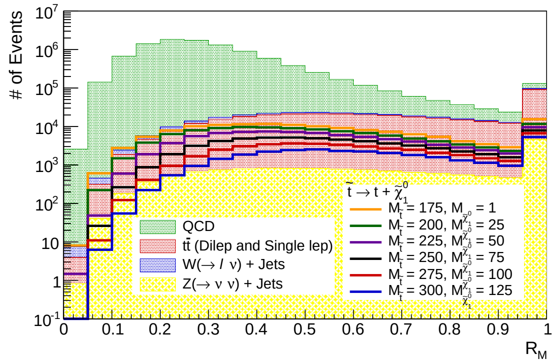

Figure 4.12: R_M distributions: After applying the initial MET $>$ 50 GeV cut (Just before selecting the ISR jet)

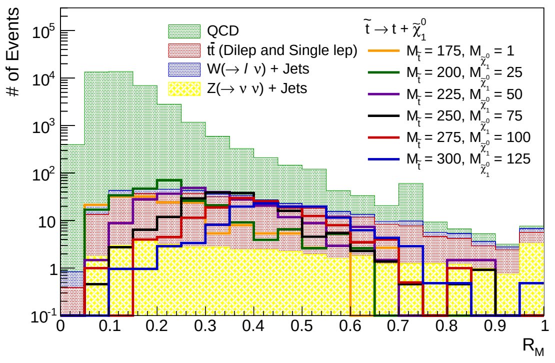

Figure 4.13: R_M distributions: After selecting the ISR jet. The peaks are clearly distinguishable for every signal point

$\mathscr{L}$ is the integrated luminosity, σ is the cross section of the signal process and R is the fraction of the events selected from the total number produced, which is $\mathscr{L} * \sigma$. As $\mathscr{L}$ and R are the same for expected and observed events, the r value can also be written as:

$$r = \frac{\sigma_{Observed}}{\sigma_{Theoretical}} \tag{4.2}$$

where $\sigma_{Observed}$ is the observed cross-section of the signal process and $\sigma_{Theoretical}$ is the theoretically calculated cross-section of the signal process. Hence, the limit on r will also provide an

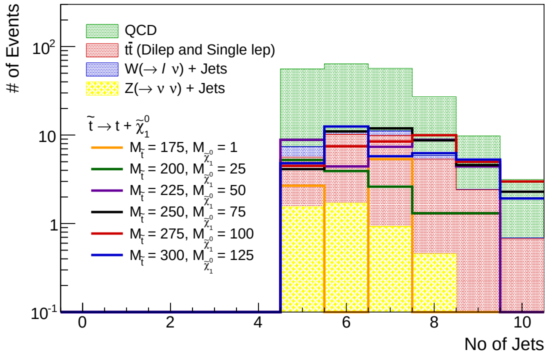

Figure 4.14: Jet Multiplicity Distributions: After applying the $\Delta\phi(MET, jet) > 0.3$ selection.

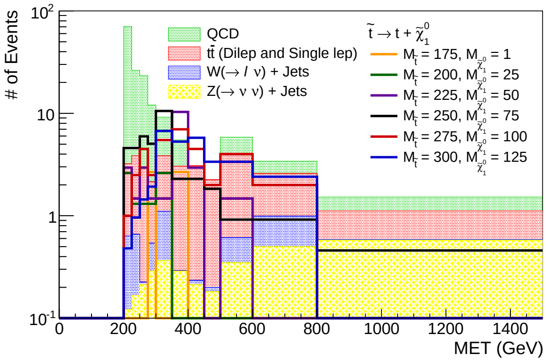

Figure 4.15: MET distributions: After applying all the selection criteria with MET> 200 GeV selection

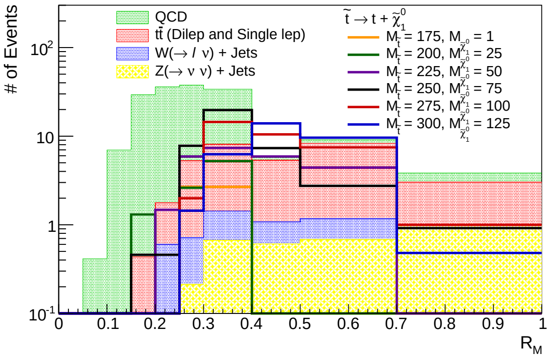

Figure 4.16: R_M distributions: After applying all the selection criteria with MET> 200 GeV selection

upper limit on the cross-section of the signal process.

A tool is developed by the CMS collaboration to calculate the limits, when data, MC background and signal events survived after the event selection are provided. The methods of statistics used for limit calculation are explained in[37] [38] [39] [40]. Here, the number of observed events provided is equal to the number of total background events. If the upper limit calculated on r is lesser than 1, then it means that the cross-section calculated is greater than the one observed. It is a clear exclusion of that signal model. For calculating these limits, the observed data was assumed

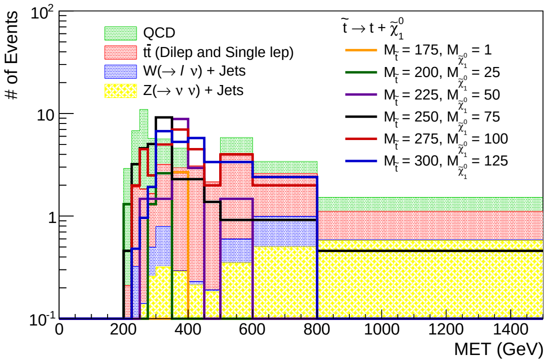

Figure 4.17: MET distributions: After applying all the selection criteria with $R_M > 0.3$ selection

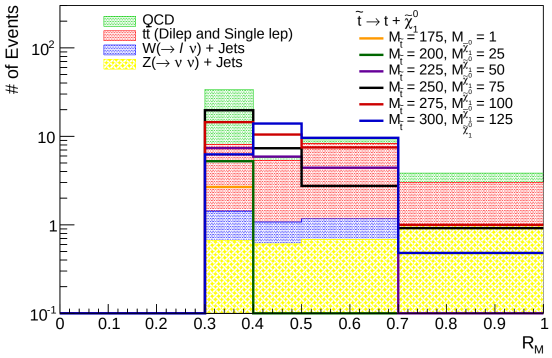

Figure 4.18: R_M distributions: After applying all the selection criteria with $R_M > 0.3$ selection

to be equal to the number of background events, as the study of data is out of the scope of this thesis. The limits have been calculated using 11 search regions in MET and 4 search regions in R_M and assuming 20% systematics + MC statistical errors. The tables 4.2, 4.3 and 4.4 provide the number of events survived after applying the entire event selection and also provide the upper limits on r for the model points of stop for the assumed luminosities of 30 fb^{-1}, 35.9 fb^{-1} and 100 fb^{-1}, respectively. The luminosity of 35.9 fb^{-1} is the current luminosity at the LHC recorded by the CMS experiment. The collaboration expects to record a $\mathscr{L} \approx 100$ fb^{-1} by the end of year 2017.

The channels mentioned in the tables have been selected after looking at the upper limits on r for $M_{\tilde{t}} \geqslant$225 GeV, which can increase the sensitivity of this analysis for the exclusion study. For a given luminosity, the limits calculated for the selected channels are not significantly different, but as can be seen from the table 4.2, the QCD events are reduced to a greater extent in the channel $R_M > 0.3$ and $MET > 300$ GeV. To reduce the uncertainties on QCD background, which depend on the number of events survived, it is advisable to have lesser number of QCD events for more precise measurements of the background uncertainties. The number of QCD events is lower in

Process	MET>200 GeV	MET>300 GeV	$R_M > 0.3$, MET>300 GeV	$R_M > 0.3$
QCD	129	10.7	7.08	26.9
TTbar	26.0	15.9	15.4	20.0
W+Jets	2.82	1.55	1.25	1.72
Z+Jets	3.23	2.44	2.40	2.92
Total Background	161	30.7	26.1	50.7
$(M_{\tilde{t}}, M_{\tilde{\chi}_1^0})$				
(175,1)	5.36 ($r < 3.16$)	2.68 ($r < 4.04$)	2.68 ($r < 3.74$)	2.68($r < 12.22$)
(200,25)	9.15 ($r < 4.19$)	2.62 ($r < 4.33$)	2.62 ($r < 3.47$)	5.23($r < 4.42$)
(225,50)	25.0 ($r < 0.67$)	16.2 ($r < 0.68$)	14.7 ($r < 0.73$)	17.7($r < 1.15$)
(250,75)	39.4 ($r < 0.69$)	19.3 ($r < 0.74$)	17.4 ($r < 0.70$)	30.7($r < 0.70$)
(275,100)	35.4 ($r < 0.62$)	24.9 ($r < 0.65$)	24.4 ($r < 0.61$)	33.4($r < 0.56$)
(300,125)	31.3 ($r < 0.56$)	26.5 ($r < 0.59$)	26.5 ($r < 0.54$)	29.8($r < 0.43$)
(400,225)	16.8 ($r < 0.58$)	16.8 ($r < 0.59$)	16.8 ($r < 0.58$)	16.8($r < 0.66$)
(425,250)	13.4 ($r < 0.84$)	13.4 ($r < 0.86$)	13.4 ($r < 0.86$)	13.4($r < 0.79$)
(450,275)	8.19 ($r < 1.50$)	8.19 ($r < 1.55$)	8.19 ($r < 1.55$)	8.19($r < 1.31$)
(475,300)	6.67 ($r < 1.67$)	6.67 ($r < 1.72$)	6.67 ($r < 1.71$)	6.67($r < 1.69$)
(500,325)	3.20 ($r < 4.56$)	3.43 ($r < 4.77$)	3.43 ($r < 4.74$)	3.43($r < 3.36$)

Table 4.2: Expected Upper Limit on r value for the luminosity of 30 fb^{-1} and also the number of events survived for all the processes for different channels (a)$MET > 200$ GeV, (b)$MET > 300$ GeV, (c)$R_M > 0.3$ and $MET > 300$ GeV (d)$R_M > 0.3$. 20% systematics are used.

the case, where '$MET > 300$ GeV' approximately by 92% compared to the case of '$MET > 200$ GeV' and further reduced by 30% in case of '$R_M >$0.3, MET $>$ 300 GeV'. The combination of R_M and MET selection results in a better control over the QCD background events.

Although the analysis provides good limits for the stop models with $M_{\tilde{t}} \geqslant$225 GeV, the analysis using ISR tagging as the strategy is not sensitive enough for probing the signal model points, where $M_{\tilde{t}} <$225 GeV. This can be due to the selection on MET or R_M which essentially puts a higher threshold on MET removing the events with lower MET and hence the events with LSP masses closer to zero are rejected. Also the limits were calculated for the models with $M_{\tilde{t}} > 300$ GeV, which have been excluded by previous CMS analyses [18]. The analysis is not sensitive for $M_{\tilde{t}} \geqslant 450$ GeV. The cross-section is decreased with an increase in the stop mass. So, applying

Process	MET>200 GeV	MET>300 GeV	$R_M > 0.3$, MET>300 GeV	$R_M > 0.3$
QCD	155	12.9	8.47	32.7
TTbar	31.2	19.1	18.4	24.0
W+Jets	3.37	1.85	1.50	2.06
Z+Jets	3.87	2.93	2.87	3.49
Total Background	193	36.8	31.2	62.3
$(M_{\tilde{t}}, M_{\tilde{\chi}_1^0})$				
(175,1)	6.41 ($r < 2.87$)	3.20 ($r < 3.64$)	3.20 ($r < 3.36$)	3.20($r < 11.84$)
(200,25)	11.0 ($r < 3.83$)	3.13 ($r < 3.95$)	3.13 ($r < 3.14$)	6.26($r < 4.27$)
(225,50)	30.0 ($r < 0.61$)	19.4 ($r < 0.62$)	17.6 ($r < 0.67$)	21.2($r < 1.07$)
(250,75)	47.2 ($r < 0.63$)	23.0 ($r < 0.68$)	20.8 ($r < 0.64$)	36.8($r < 0.66$)
(275,100)	42.4 ($r < 0.57$)	29.8 ($r < 0.61$)	29.2 ($r < 0.57$)	40.0($r < 0.52$)
(300,125)	37.4 ($r < 0.52$)	31.7 ($r < 0.54$)	31.7 ($r < 0.50$)	35.7($r < 0.40$)
(400,225)	20.1 ($r < 0.53$)	20.1 ($r < 0.53$)	20.1 ($r < 0.53$)	20.1($r < 0.60$)
(425,250)	16.0 ($r < 0.76$)	16.0 ($r < 0.79$)	13.4 ($r < 0.79$)	16.0($r < 0.72$)
(450,275)	9.80 ($r < 1.37$)	9.80 ($r < 1.42$)	8.19 ($r < 1.43$)	9.80($r < 1.19$)
(475,300)	7.98 ($r < 1.52$)	7.98 ($r < 1.57$)	6.67 ($r < 1.57$)	7.98($r < 1.54$)
(500,325)	4.11 ($r < 4.17$)	4.11 ($r < 4.39$)	3.43 ($r < 4.36$)	4.11($r < 3.05$)

Table 4.3: The number of events survived for all the processes for different channels (a)$MET > 200$ GeV, (b)$MET > 300$ GeV, (c)$R_M > 0.3$ and $MET > 300$ GeV (d)$R_M > 0.3$ along with the expected Upper Limit on r given in the brackets for the luminosity of 100 fb^{-1}. 20% systematics are used.

further selection along with ISR tagging results in low signal acceptance.

The tables 4.2, 4.3 and 4.4 for luminosities equal to 30 fb^{-1}, 35.9 fb^{-1} and 100 fb^{-1}, respectively, show that the limits are improved with an increase in the luminosity. The upper limits on r are improved by approximately 35-45 % from $\mathscr{L} = 30$ fb^{-1} to $\mathscr{L} = 100$ fb^{-1} for the channel $R_M > 0.3$ and $MET > 300$ GeV. Figures 4.19, 4.20 and 4.21 also show that the limits on cross-sections of different stop masses are improved with an increase in the luminosity.

Process	MET>200 GeV	MET>300 GeV	$R_M > 0.3$, MET>300 GeV	$R_M > 0.3$
QCD	432	35.9	23.6	90.6
TTbar	86.8	53.1	51.3	66.8
W+Jets	9.39	5.15	4.16	5.75
Z+Jets	10.8	8.15	8.00	9.72
Total Background	539	102	87	173
($M_{\tilde{t}}$, $M_{\tilde{\chi}_1^0}$)				
(175,1)	17.9 ($r < 1.66$)	8.93 ($r < 1.66$)	8.93 ($r < 1.93$)	8.93 ($r < 9.53$)
(200,25)	30.5 ($r < 2.26$)	8.72 ($r < 2.26$)	8.72 ($r < 1.82$)	17.4 ($r < 3.42$)
(225,50)	83.5 ($r < 0.35$)	54.1 ($r < 0.35$)	49.1 ($r < 0.39$)	59.0 ($r < 0.71$)
(250,75)	131 ($r < 0.40$)	64.2 ($r < 0.40$)	58.1 ($r < 0.40$)	102 ($r < 0.47$)
(275,100)	118 ($r < 0.39$)	83.1 ($r < 0.39$)	81.5 ($r < 0.39$)	111 ($r < 0.35$)
(300,125)	104 ($r < 0.35$)	88.2 ($r < 0.35$)	88.2 ($r < 0.35$)	99.4 ($r < 0.25$)
(400,225)	56.0 ($r < 0.32$)	56.0 ($r < 0.32$)	56.0 ($r < 0.31$)	56.0 ($r < 0.38$)
(425,250)	44.7 ($r < 0.46$)	44.7 ($r < 0.46$)	44.7 ($r < 0.47$)	44.7 ($r < 0.45$)
(450,275)	27.3 ($r < 0.84$)	27.3 ($r < 0.84$)	27.3 ($r < 0.89$)	27.3 ($r < 0.72$)
(475,300)	22.2 ($r < 0.91$)	22.2 ($r < 0.91$)	22.2 ($r < 0.95$)	22.2 ($r < 0.96$)
(500,325)	11.4 ($r < 2.63$)	11.4 ($r < 2.63$)	11.4 ($r < 2.82$)	11.5 ($r < 1.85$)

Table 4.4: The number of events survived for all the processes for different channels (a)$MET > 200$ GeV, (b)$MET > 300$ GeV, (c)$R_M > 0.3$ and $MET > 300$ GeV (d)$R_M > 0.3$ along with the expected Upper Limit on r given in the brackets for the luminosity of 100 fb^{-1}. 20% systematics are used.

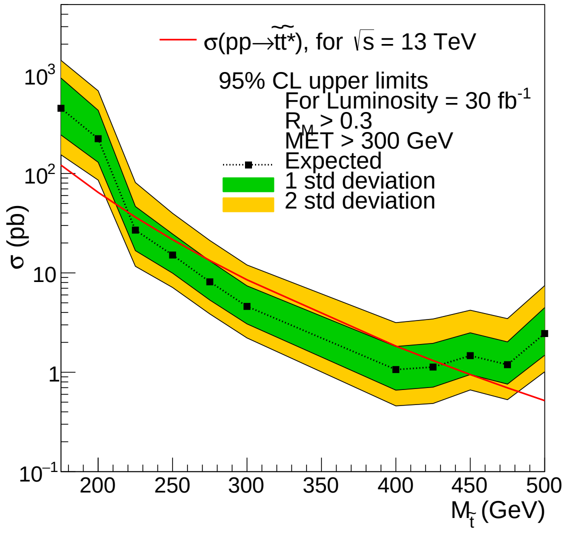

Figure 4.19: Upper Limit on cross section at 95% CL versus the stop mass in GeV. $\mathscr{L} = 30\ \text{fb}^{-1}$ with 20% systematics

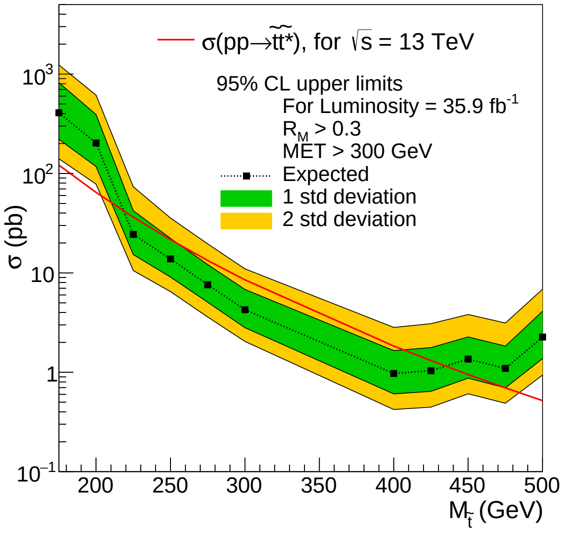

Figure 4.20: Upper Limit on cross section at 95% CL versus the stop mass in GeV. $\mathscr{L} = 35.9\ \text{fb}^{-1}$ with 20% systematics

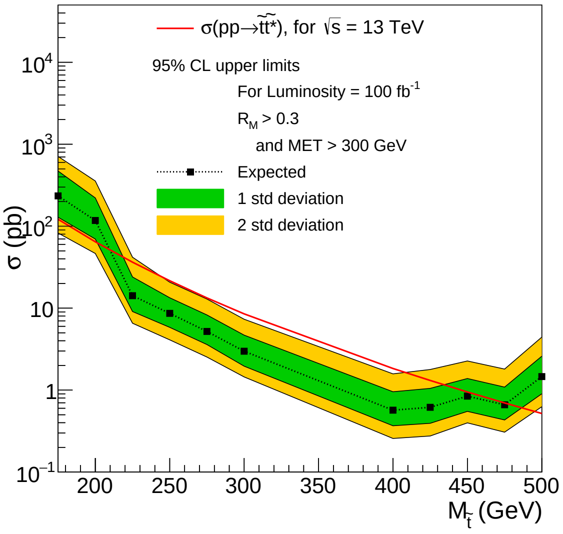

Figure 4.21: Upper Limit on cross section at 95% CL versus the stop mass in GeV. $\mathscr{L} = 100\ \text{fb}^{-1}$ with 20% systematics

Chapter 5

Stop search using di-leptonic final state

5.1 Baseline Selection

To develop an analysis strategy based on dilepton events, a CMS study [41] is referred for deciding the event selection criteria. The MET distributions for stop events and SM backgrounds before applying any selection and after applying the filters are shown in figures 5.1 and figure 5.2 respectively (explained in section 4.1).

This analysis is based on two leptons in the final state, which could be $\mu\mu$ or ee or $e\mu$. As these two leptons originate from the two W bosons decaying from two tops, they should have opposite signs. These muons should have $p_T > 20$ GeV, $|\eta| < 2.4$ and Mini-Isolation < 0.1 and electrons should have $p_T > 20$ GeV, $|\eta| < 2.5$ and Mini-Isolation < 0.1. Also, a third muon (electron) is vetoed, if it satisfies $p_T > 15$ GeV, $|\eta| < 2.4$ ($|\eta| < 2.5$) and Mini-Isolation < 0.4. See figure 5.3 for the MET distributions after selecting the opposite-sign leptons.

Since targeted signal has two top quarks in the final state, there should be at least two jets with $p_T > 30$ GeV and $|\eta| < 2.4$ in the events. The MET distributions after the jet requirements are

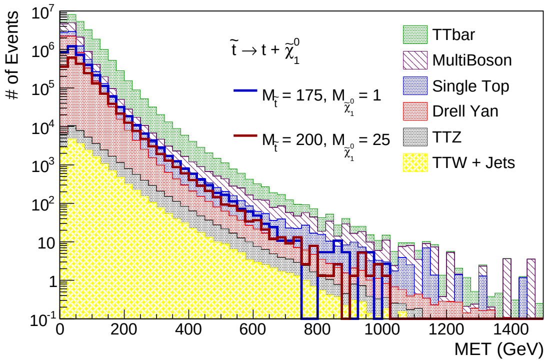

Figure 5.1: MET distributions: Before applying any selection

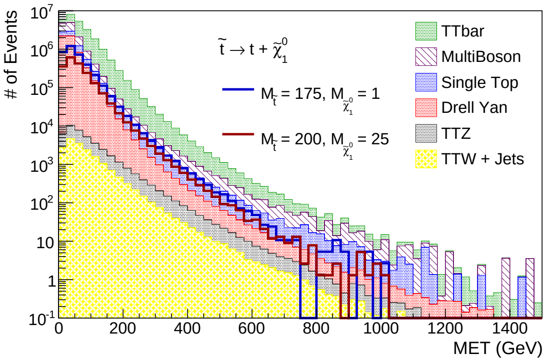

Figure 5.2: MET distributions: After applying High MET Filters

shown in figure 5.4. At least two leading jets among the selected jets should be b-tagged jets. As seen from figure 5.5, the background is dominated by $t\bar{t}$ events after requiring two b-tagged jets.

The minimum dilepton invariant mass of the two leptons is required to be 20 GeV. This selection is mainly relevant for data and does not affect the distributions in MC as observed in figure 5.6. To reduce the background from Z to ll, the magnitude of the difference between the invariant mass of the two leptons and Z mass should be greater than 15 GeV. As seen in figure 5.7, the Z mass window cut does not have much effect on the MET distributions. The requirement of two b-tagged jets already rejects most of the background events containing Z to ll process.

A selection of $MET > 30$ GeV for di-muon or di-electron events and $MET > 20$ GeV for the $e\mu$ events is applied. The figure 5.8 shows MET distributions after applying this criterion.

5.2 $M_{t\bar{t}}$ reconstruction using parton level neutrinos

As discussed in section 3.3, the discriminating power of the spin correlations between the two leptons in $t\bar{t}$ or $\tilde{t}\tilde{t}^*$ events depends on the boost of the top quarks according to the generator level study. The invariant mass of the $t\bar{t}$ system ($M_{t\bar{t}}$) is a good experimental handle to select the events

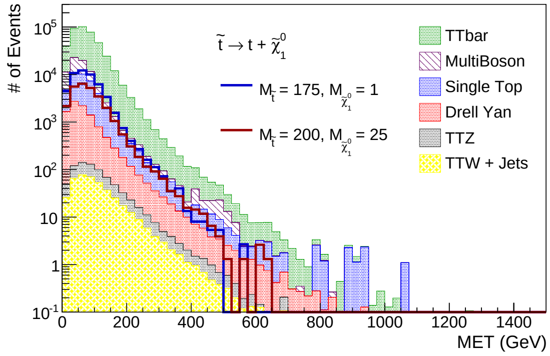

Figure 5.3: MET distributions: After selecting oppositely charged leptons

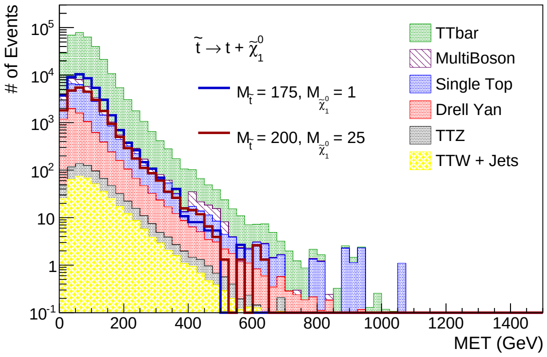

Figure 5.4: MET distributions: After applying Njets $\geqslant 2$ criterion

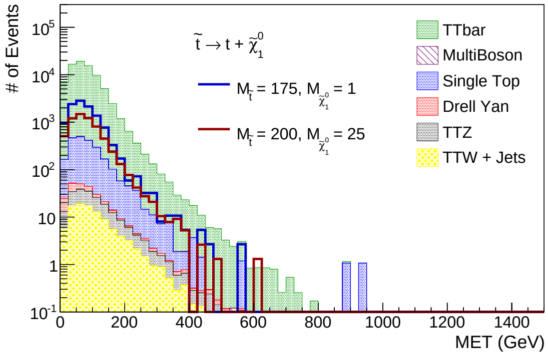

Figure 5.5: MET distributions: After applying No of b-jets $\geqslant 2$ criterion

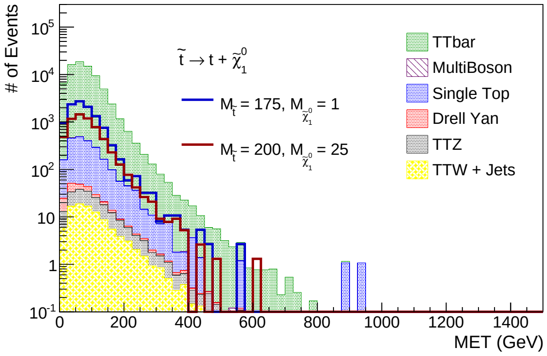

Figure 5.6: MET distributions: After applying $M_{ll} > 20$ GeV

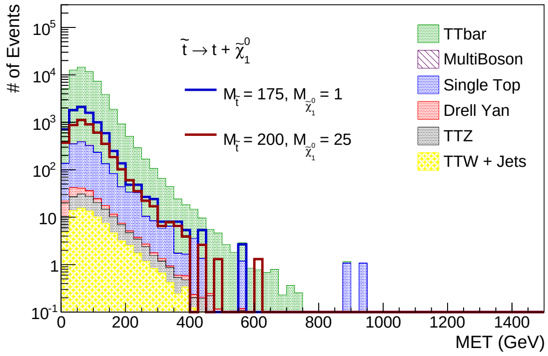

Figure 5.7: MET distributions: After applying $|M_{ll} - M_Z| > 15$ GeV

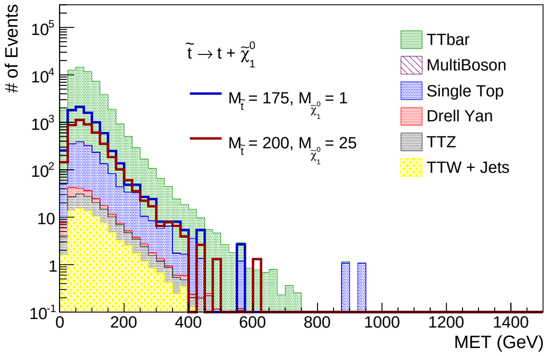

Figure 5.8: MET distributions: After applying MET cut

with different range of boosts. Performing a complete top mass reconstruction in dilepton events,

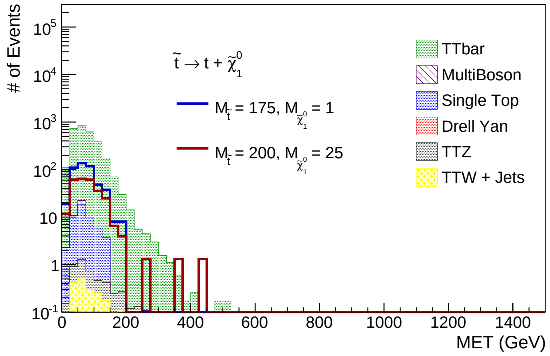

Figure 5.9: MET distributions: After reconstructing both the tops with the criteria given in the description (See section 5.1)

which uses MET, is beyond the scope of this study. However, we can study the potential of this approach using the generated neutrinos to reconstruct the four-momenta of top candidates, and $M_{t\bar{t}}$. All other variables referring to jets, b-tagged jets, MET and leptons used in the following study are reconstructed quantities including all the detector level effects.

Different combinations of the two leptons (l_1, l_2), two b-tagged jets (j_1, j_2) and two generator level neutrinos (n_1, n_2) decaying from the two W bosons are used to reconstruct the best top candidates. The combinations having the minimum difference in the reconstructed top masses and also the combinations with reconstructed masses satisfying $|RecoTopmass_1 - RecoTopMass_2| < 3$ GeV are selected. Using four momenta of these reconstructed top quarks, the $M_{t\bar{t}}$ is calculated. See figures 5.10 and 5.11 for the reconstructed top mass distributions and for the $M_{t\bar{t}}$ distributions, respectively. The top mass distributions are consistent with the known and measured mass of top, which is approximately 173.2 GeV [32].

All the selected events have been divided into two categories: (1) $M_{t\bar{t}} \leqslant 450$ GeV, and (2) $M_{t\bar{t}} > 450$ GeV to separate a sample of events with less boosted top quarks from boosted top quarks. See figures 5.12, 5.13 and 5.14 for the $\Delta\phi(l_1, l_2)$ distributions with inclusive in $M_{t\bar{t}}$, $M_{t\bar{t}} \leqslant 450$ GeV and $M_{t\bar{t}} \geq 450$ GeV, respectively. These do not show any particular significant change in the behaviour

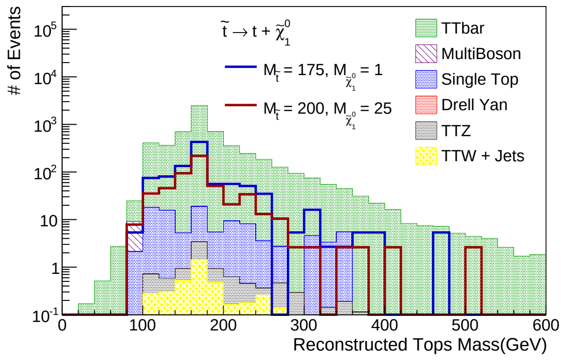

Figure 5.10: Reconstructed top mass distributions for both the tops

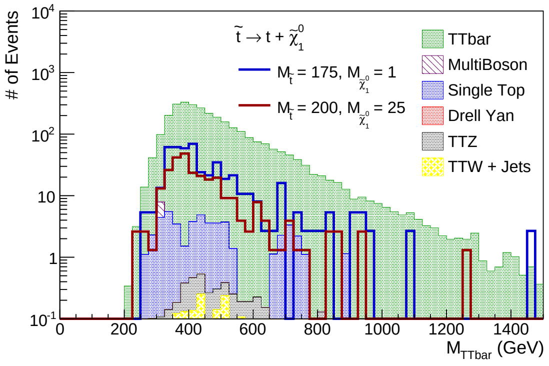

Figure 5.11: Invariant mass of reconstructed $t\bar{t}$

of the signal distributions from the background ones and are completely dominated by the $t\bar{t}$ events because of its high cross-section. The table 5.1 can be referred for th number of events survived after every selection for the dilepton analysis.

However, if the stop events are produced in the p-p collisions, the overall number of dilepton events selected will be in excess to those expected from the SM $t\bar{t}$ production. As observed in figures 5.12, 5.13 and 5.14, this excess would be uniformly spread across the $\Delta\phi(l_1, l_2)$ distribution. Therefore, we investigate the ratio of the number of signal+background events to the number of background events. This ratio should be more than unity, if there exists some signal. Here are some distributions (See figures 5.16 and 5.17) of signal, where $M_{\tilde{t}} = 175$ GeV and $M_{\tilde{t}} = 200$ GeV with the (S+B)/B ratio distributions. Also, the distributions of the events are divided into the two categories (based on $M_{t\bar{t}}$ of $t\bar{t}$) mentioned above (See figures 5.18, 5.19, 5.20 and 5.21). The legend used for these distributions is given in figure 5.15. Even if this value is greater than unity, the uncertainties on this ratio will determine, if there is a possibility of existence of the signal.

Selection	$t\bar{t}$	**Drell-Yan**	**Single Top (tW channel)**	**TTW + Jets**	**TTZ**	**Multiboson**	**Total Bkg**	**(175,1)**	**(200, 25)**
No cut	13357797	5887978	2135998	18314	23477	5366628	22652612	3642480	1935253
MET Filters	13313381	5862176	2128717	18241	23390	5347831	22569375	3630222	1928572
Selecting two opposite sign leptons	335850	9365	30839	413	353	35903	205209	50506	27321
Njets $\geqslant 2$	292116	6825	19442	401	343	7326	144732	43417	23556
N-bjets $\geqslant 2$	75917	60	2035	101	106	16	31003	11217	6247
$M_{ll} > 20$ **GeV**	73797	59	1991	99	104	16	30219	10942	6064
$\lvert M_{ll} - M_Z \rvert > 15$ **GeV**	57413	56	1575	81	83	16	23243	8376	4678
MET > 30 **GeV (for** ee **or** $\mu\mu$**) & MET** > 20 **GeV (for** $e\mu$**)**	54156	48	1505	77	79	16	22022	7921	4451
Top Mass Reconstruction	2951	0	47	2	2	3	1298	484	273

Table 5.1: Cutflow table for all the selections applied in the dilepton analysis

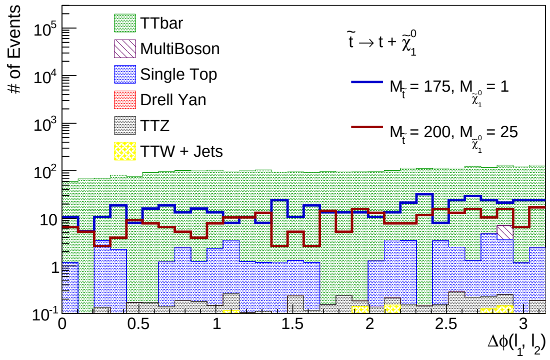

Figure 5.12: $\Delta\phi(l_1, l_2)$ distributions for inclusive $M_{t\bar{t}}$.

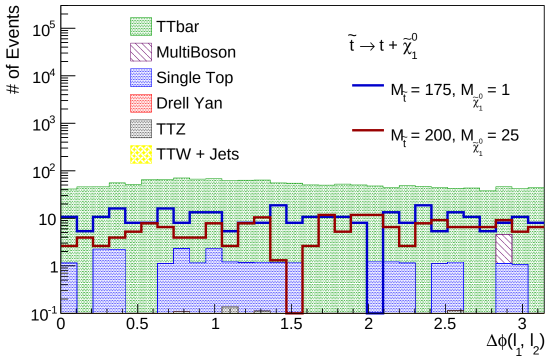

Figure 5.13: $\Delta\phi(l_1, l_2)$ distributions for $M_{t\bar{t}} \leqslant 450$ GeV.

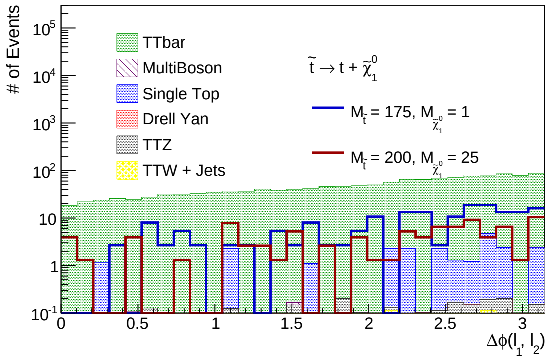

Figure 5.14: $\Delta\phi(l_1, l_2)$ distributions for $M_{t\bar{t}} > 450$ GeV.

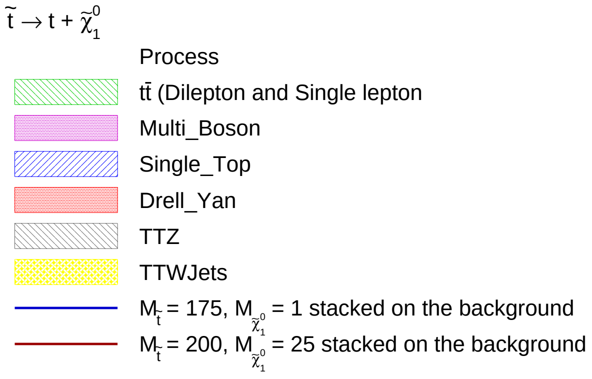

Figure 5.15: The Legend for all the Ratio-Plots in figures 5.16 5.17 5.18 5.19 5.20 5.21.

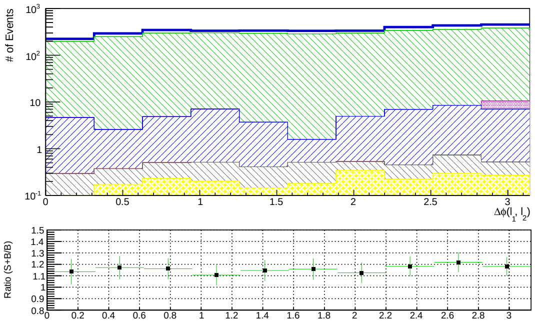

Figure 5.16: $\Delta\phi(l_1, l_2)$ distributions for $M_{\tilde{t}} = 175$ GeV with the (Signal+Background)/Background ratio plots given below (Inclusive $M_{t\bar{t}}$ events)

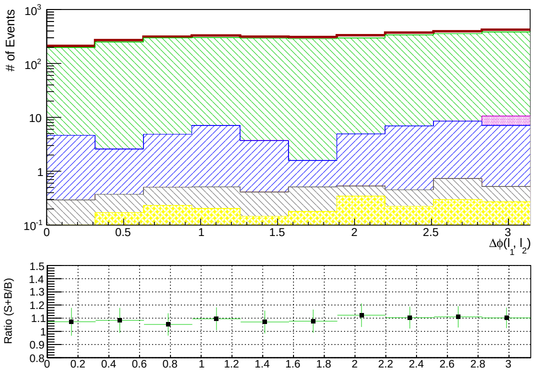

Figure 5.17: $\Delta\phi(l_1, l_2)$ distributions for $M_{\tilde{t}} = 200$ GeV with the (Signal+Background)/Background ratio plots given below (Inclusive $M_{t\bar{t}}$ events)

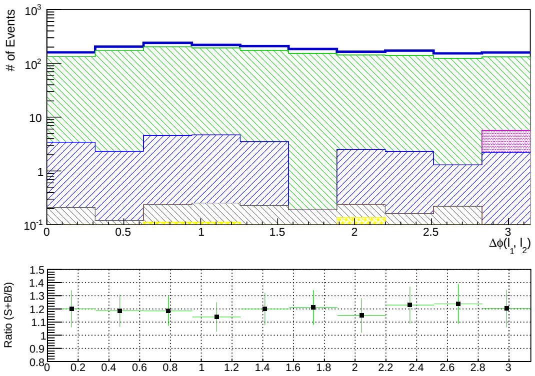

Figure 5.18: $\Delta\phi(l_1, l_2)$ distributions for $M_{\tilde{t}} = 175$ GeV with the (Signal+Background)/Background ratio plots given below ($M_{t\bar{t}} \leqslant 450$ GeV events)

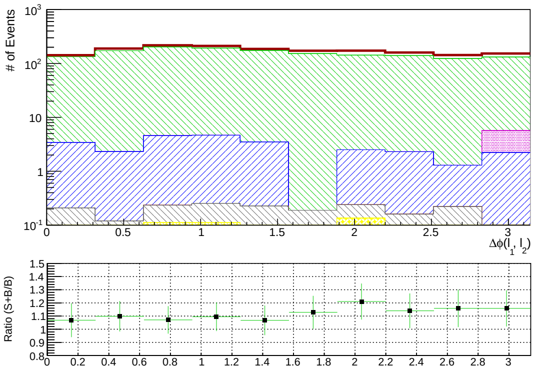

Figure 5.19: $\Delta\phi(l_1, l_2)$ distributions for $M_{\tilde{t}} = 200$ GeV with the (Signal+Background)/Background ratio plots given below ($M_{t\bar{t}} \leqslant 450$ GeV events)

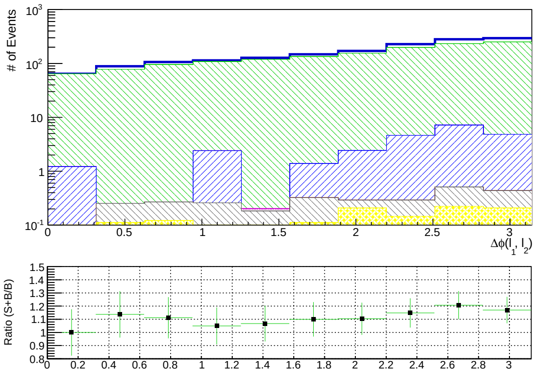

Figure 5.20: $\Delta\phi(l_1, l_2)$ distributions for $M_{\tilde{t}} = 175$ GeV with the (Signal+Background)/Background ratio plots given below ($M_{t\bar{t}} > 450$ GeV events)

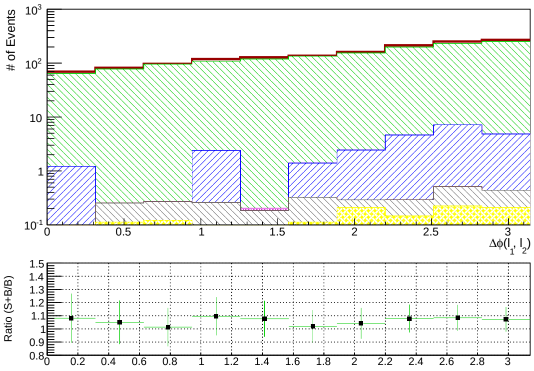

Figure 5.21: $\Delta\phi(l_1, l_2)$ distributions for $M_{\tilde{t}} = 200$ GeV with the (Signal+Background)/Background ratio plots given below ($M_{t\bar{t}} > 450$ GeV events)

5.3 Results and discussion for Dilepton analysis

The upper limits on r for 95% confidence limit are calculated for the dilepton analysis, where r is defined in equation 4.1.

Signal	Inclusive $M_{t\bar{t}}$	$M_{t\bar{t}} \leqslant 450$ GeV	$M_{t\bar{t}} > 450$ GeV	$R_M > 0.3$, $MET > 300$ GeV
($M_{\tilde{t}}$, $M_{\tilde{\chi}_1^0}$)	Expected upper limit on r with 95% CL for 20% systematics			
(175,1)	1.24	1.62	0.99	3.74
(200,25)	2.04	1.14	1.87	3.47

Table 5.2: Expected Upper Limit on r value for the luminosity of 30 fb^{-1} using the events in the entire range of $\Delta\phi(l_1, l_2)$ (a)Inclusive $M_{t\bar{t}}$, (b)$M_{t\bar{t}} \leqslant 450$ GeV, (c)$M_{t\bar{t}} > 450$ GeV and comparison of all these upper limits with those for the channel in the full hadronic analysis i.e. $R_M > 0.3$, $MET > 300$ GeV.

Signal	Inclusive $M_{t\bar{t}}$	$M_{t\bar{t}} \leqslant 450$ GeV	$M_{t\bar{t}} > 450$ GeV	$R_M > 0.3$, $MET > 300$ GeV
($M_{\tilde{t}}$, $M_{\tilde{\chi}_1^0}$)	Expected upper limit on r with 95% CL for 20% systematics (for 10% systematics)			
(175,1)	1.16 (0.87)	1.56 (1.01)	0.91 (0.80)	3.36
(200,25)	1.91 (1.46)	1.06 (0.91)	1.71 (1.56)	3.14

Table 5.3: Expected Upper Limit on r value for the luminosity of 35.9 fb^{-1} using the events in the entire range of $\Delta\phi(l_1, l_2)$ (a)Inclusive $M_{t\bar{t}}$, (b)$M_{t\bar{t}} \leqslant 450$ GeV, (c)$M_{t\bar{t}} > 450$ GeV and comparison of all these upper limits with those for the channel in the full hadronic analysis i.e. $R_M > 0.3$, $MET > 300$ GeV.

Signal	Inclusive $M_{t\bar{t}}$	$M_{t\bar{t}} \leqslant 450$ GeV	$M_{t\bar{t}} > 450$ GeV	$R_M > 0.3$, $MET > 300$ GeV
($M_{\tilde{t}}$, $M_{\tilde{\chi}_1^0}$)	Expected upper limit on r with 95% CL for 20% systematics (for 10% systematics)			
(175,1)	0.77 (0.65)	1.19 (0.87)	0.56 (0.52)	1.93
(200,25)	1.25 (1.07)	0.67 (0.61)	1.06 (1.00)	1.82

Table 5.4: Expected Upper Limit on r value for the luminosity of 100 fb^{-1} using the events in the entire range of $\Delta\phi(l_1, l_2)$ (a)Inclusive $M_{t\bar{t}}$, (b)$M_{t\bar{t}} \leqslant 450$ GeV, (c)$M_{t\bar{t}} > 450$ GeV and comparison of all these upper limits with those for the channel in the full hadronic analysis i.e. $R_M > 0.3$, $MET > 300$ GeV.

The limits calculated using $\mathscr{L} = 30$ fb^{-1} for the di-lepton analysis are better than the ones calculated for the channel $R_M > 0.3$, $MET > 300$ GeV in full hadronic analysis by approximately a factor of 3. This can be seen in table 5.2 and also can be observed for other integrated luminosities shown in tables 5.3 and 5.4. In all the limit plots presented in this section, the upper limits with 1σ and 2σ bands for $M_{\tilde{t}} \leqslant 200$ GeV are plotted using upper limits calculated for the dilepton analysis and for rest of the stop masses, the limit values are calculated using the full hadronic analysis. Figure 5.22 shows the plot of expected limits on cross-sections calculated for $\mathscr{L} = 30$ fb^{-1}. Also, as the luminosity is increased, the limits improve (See tables 5.3 and 5.4). For example, in the $M_{t\bar{t}} \leqslant 450$ GeV channel , the limits improve approximately by 27% going from $\mathscr{L} = 30$ fb^{-1} to $\mathscr{L} = 100$ fb^{-1} for $M_{\tilde{t}} = 175$ GeV and by approximately 41% for $M_{\tilde{t}} = 200$ GeV. The improvement in the limits on cross-sections can also be seen in figures 5.23 and 5.24.

Also, the limits of the cross-sections can further be improved with the control on the uncertainties. The systematic uncertainties used are 10% in the figures 5.25 and 5.26. The improvement in the limits can be noted compared to the previous limits with 20% systematic uncertainties. The limits on r are improved by approximately 35% in $M_{t\bar{t}} \leqslant 450$ GeV channel in case of $\mathscr{L} = 35.9$ fb^{-1} for $M_{\tilde{t}} = 175$ GeV and by 14% for $M_{\tilde{t}} = 200$ GeV. These results are also evident in figure

One of the limitation of this analysis is the consideration of generator level neutrinos for the top mass reconstruction. The MET measured has to be used for the reconstruction of both the tops. Even though the use of generator level neutrinos might give overly realistic results, the potential of this analysis could be explored. Also the potential of the different $M_{t\bar{t}}$ channels selected for the limit calculation can be further explored. The distinction clearly seen in the generator level plots for the channel $M_{t\bar{t}} \leqslant 450 GeV$, gets washed out in the reconstruction level plots after the selection has been applied. The current choice on lepton selections can be optimized further to go as close as possible to generator level selections.

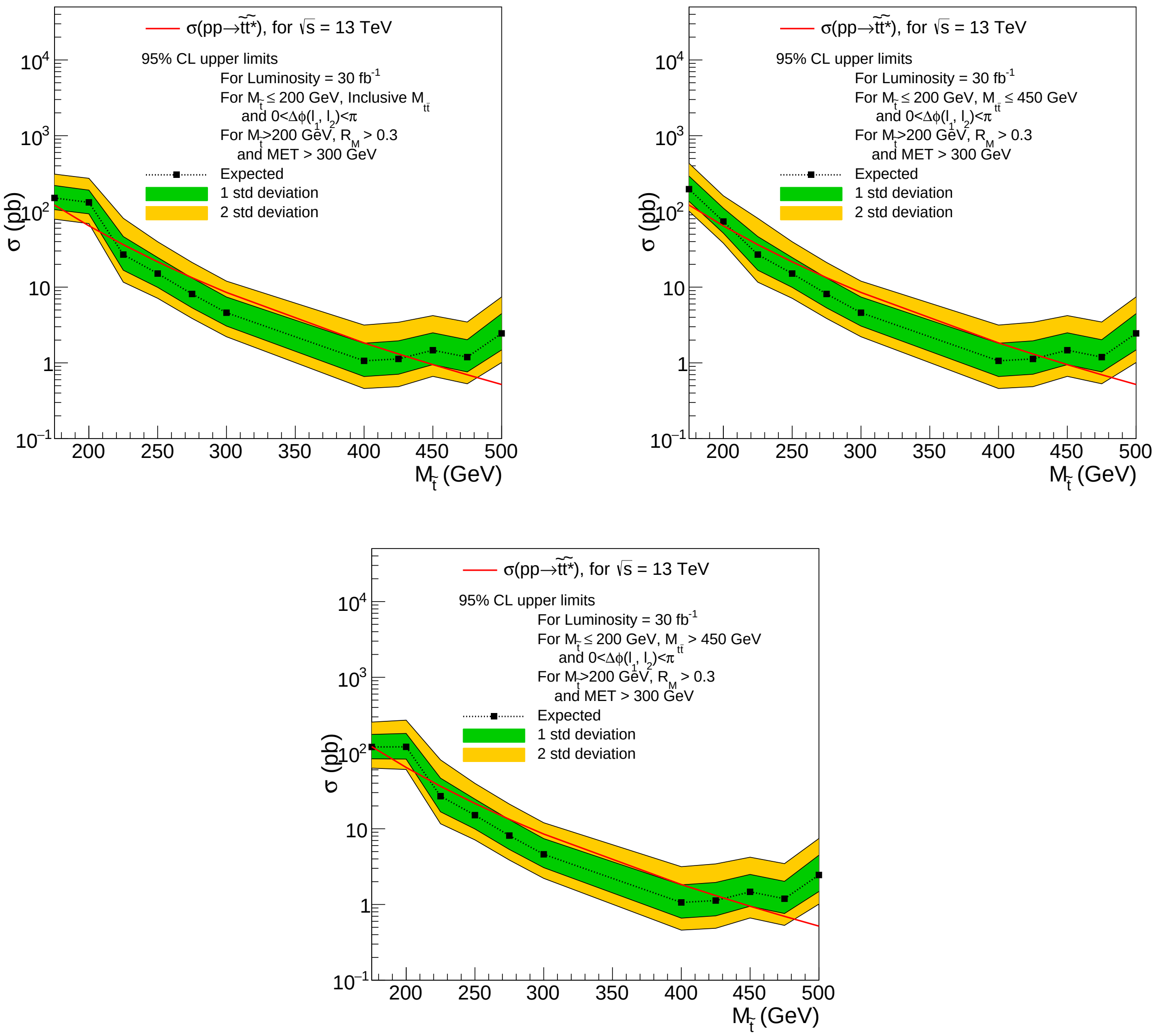

Figure 5.22: Upper Limit on cross section at 95% CL versus the stop mass in GeV. Luminosity = 30 fb^{-1}. The channel used is $R_M > 0.3$, $MET > 300$ GeV for $M_{\tilde{t}} \geqslant 225$ GeV ((Top Left) Inclusive $M_{t\bar{t}}$ channel for $M_{\tilde{t}} < 225$ GeV (Top Right) $M_{t\bar{t}} \leqslant 450$ GeV and (Bottom) $M_{t\bar{t}} > 450$ GeV). Systematic uncertainty used is 20%.

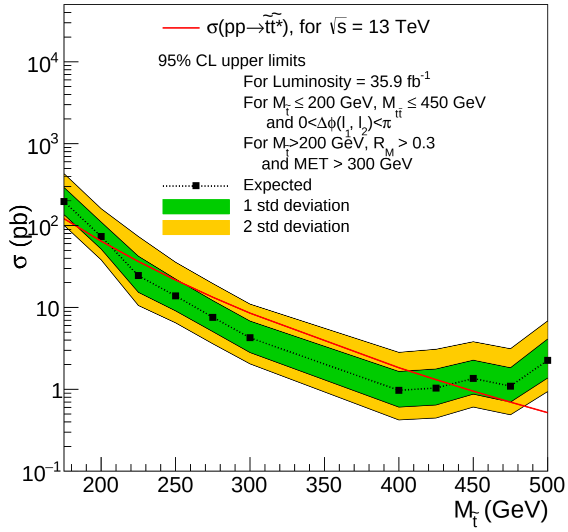

Figure 5.23: Upper Limit on cross section at 95% CL versus the stop mass in GeV. Luminosity = 35.9 fb^{-1}. ($M_{t\bar{t}} \leqslant 450$ GeV channel for $M_{\tilde{t}} < 225$ GeV and $R_M > 0.3$, $MET > 300$ GeV channel for $M_{\tilde{t}} \geqslant 225$ GeV). Systematic uncertainty used is 20%.

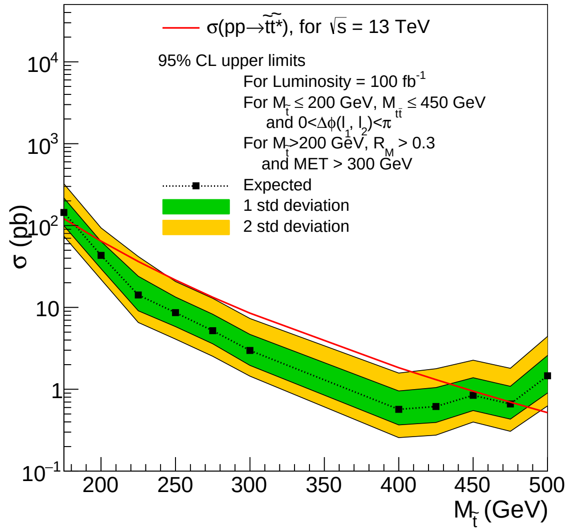

Figure 5.24: Upper Limit on cross section at 95% CL versus the stop mass in GeV. Luminosity = 100 fb^{-1} ($M_{t\bar{t}} \leqslant 450$ GeV channel for $M_{\tilde{t}} < 225$ GeV and $R_M > 0.3$, $MET > 300$ GeV channel for $M_{\tilde{t}} \geqslant 225$ GeV). Systematic uncertainty used is 20%.

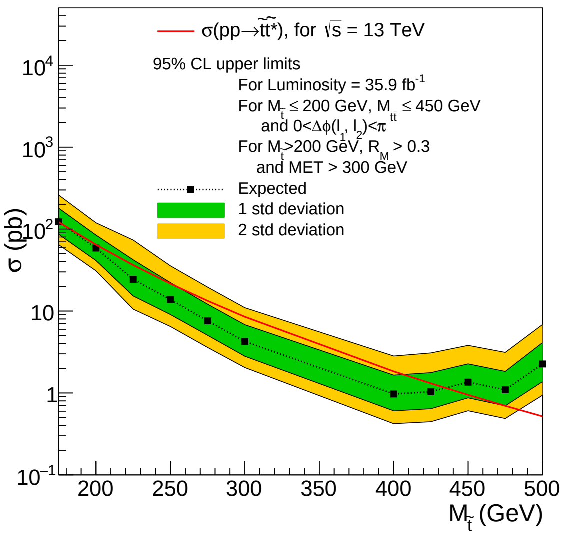

Figure 5.25: Upper Limit on cross section at 95% CL versus the stop mass in GeV. Luminosity = 35.9 fb^{-1}. ($M_{t\bar{t}} \leqslant 450$ GeV channel for $M_{\tilde{t}} < 225$ GeV and $R_M > 0.3$, $MET > 300$ GeV channel for $M_{\tilde{t}} \geqslant 225$ GeV). Systematic uncertainty used is 10%.

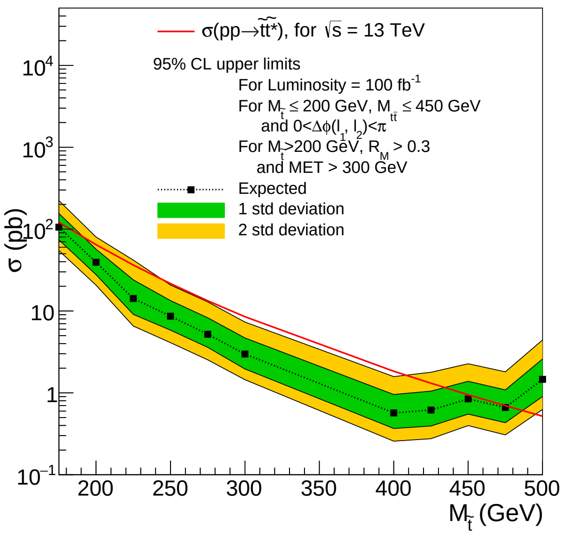

Figure 5.26: Upper Limit on cross section at 95% CL versus the stop mass in GeV. Luminosity = 100 fb^{-1}. ($M_{t\bar{t}} \leqslant 450$ GeV channel for $M_{\tilde{t}} < 225$ GeV and $R_M > 0.3$, $MET > 300$ GeV channel for $M_{\tilde{t}} \geqslant 225$ GeV). Systematic uncertainty used is 10%.

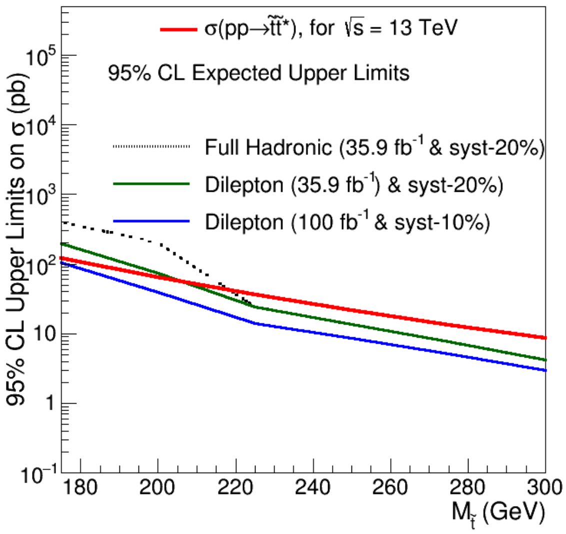

Figure 5.27: Limits on cross sections using different luminosities and systematic uncertainties for ISR tagging analysis and Dilepton analysis ($M_{\tilde{t}} = 175GeV$ and $M_{\tilde{t}} = 200GeV$)

Chapter 6

Summary and Outlook

The theory of Supersymmetry has attracted the world of physics for the several modifications it has, which try to correct the problems in the Standard Model of particle physics. It doubles the particle content of the SM and these particles being bosons for fermionic SM partners and vice versa, cancel the quantum corrections to the Higgs mass. Top quark couples to the Higgs to a greater extent because of its higher mass and also should the stop (scalar partner of top quark) if they have similar masses making stop an interesting entity to search for experimentally. The analyses developed to search for these low-mass stops in simplified models of supersymmetry are not sensitive in the region, where stop mass is closer to the top mass.

The topology studied in this thesis is $\tilde{t} \rightarrow t + \tilde{\chi}_1^0$ i.e. a stop decays into a top quark and a neutralino. Neutralino is assumed to be a weakly interacting stable particle and hence proposed to contribute to the missing transverse energy. In the top corridor region, where $M_{\tilde{t}} \approx M_t + M_{\tilde{\chi}_1^0}$, when the stop mass is closer to the top mass, it becomes difficult to probe the topology. This is because of the failure of the traditional MET based approach, which cannot differentiate between $\tilde{t}\tilde{t}^*$ and $t\bar{t}$ events as there is no extra source of missing energy due to very low MET contribution from low mass LSP.

In this thesis, two new techniques have been explored to differentiate between the $t\bar{t}$ and $\tilde{t}\tilde{t}^*$ events. One method based on the ISR jet selection is used in the full hadronic analysis of stop, which boosts the stop systems and LSPs in one direction increasing the contribution of these events to the MET. A new variable $R_M = \frac{p_T^{miss}}{p_T^{ISR}} \approx \frac{M_{\tilde{\chi}_1^0}}{M_{\tilde{t}}}$ is introduced and studied along with MET. Putting thresholds on both these variables and checking the signal acceptance along with the expected upper limit calculation using the Monte Carlo samples, showed that the stop masses in the top corridor can be excluded in the range $225 \leqslant M_{\tilde{t}} < 450$ GeV at 95% confidence level. For higher masses, the sensitivity is lower as the signal acceptance reduces to a great extent due to the low cross-sections, which adds up to the event rejection due to the ISR jet selection. For lower masses of stop ($M_{\tilde{t}} < 225$ GeV), the R_M or MET threshold is still not low enough to prevent the removal of these events.

So, another technique based on the fermionic nature of top and scalar nature of stop was studied. The spin correlation between the top quarks produced in pairs is transferred to their decay products. This shows up in the azimuthal opening angle between the two leptons in a dileptonic channel of top pair decay. The $\Delta\phi(l_1, l_2)$ distributions were studied for three different regions: inclusive in $M_{t\bar{t}}$, $M_{t\bar{t}} \leqslant 450$ GeV and $M_{t\bar{t}} \geq 450$ GeV. For the calculation of $M_{t\bar{t}}$, the top masses were reconstructed using the generator level neutrinos, reconstructed b-tagged jets and two opposite-sign leptons. The expected limits calculated at 95% confidence level for $M_{\tilde{t}} < 225$ GeV are improved with respect to the ones calculated in the full hadronic analysis (using ISR tagging), but are still not good enough for exclusion. The use of neutrinos probes the potential of this technique and motivates to use the actual top reconstruction using the MET. However, as MET is required for the actual top mass reconstruction, higher mass LSPs act as an additional source of MET making it difficult to reconstruct top masses.

The luminosities of $\mathscr{L} = 30$ fb^{-1}, 35.9 fb^{-1} (current luminosity recorded by the CMS experiment) and 100 fb^{-1} (expected to be recorded at the end of the year 2017) were used for the expected upper limit calculation. The expected upper limits on r and cross-sections show that with more statistics, it is expected to obtain better limits for both the full hadronic and di-leptonic analyses. Incorporating these techniques in the current stop searches along with the traditional approaches can improve sensitivity for the models with low stop masses in the top corridor.

Bibliography

[1] Steven Weinberg, “A Model of Leptons” Physical Review Letters. 19 (21): 12641266. doi:10.1103/PhysRevLett.19.1264

[2] A. Salam, J.C. Ward, “Electromagnetic and weak interactions”, Physics Letters Vol 13, Pages 168-171

[3] Sheldon L. Glashow, “Partial-symmetries of weak interactions”, Nucl. Phys. 22 (1961) 579-588

[4] F. Englert and R. Brout “Broken Symmetry and the Mass of Gauge Vector Mesons” Phys. Rev. Lett. 13, 321 321-323

[5] P. W. Higgs, “Broken symmetries, massless particles and gauge fields”, Phys. Lett. 12 (1964) 132.

[6] Peter W. Higgs “Broken Symmetries and the Masses of Gauge Bosons”, Physical Review Letters, Vol 13, 508, 1964

[7] P. W. Higgs, “Spontaneous Symmetry Breakdown without Massless Bosons”, Phys. Rev. 145 (1966) 1156.

[8] T. W. B. Kibble, “Symmetry Breaking in Non-Abelian Gauge Theories”, Phys. Rev. 155 (1967) 1554.

[9] ATLAS Collaboration “Observation of a new particle in the search for the Standard Model Higgs boson with the ATLAS detector at the LHC” Phys. Lett. B726 (2013) 1-29

[10] CMS Collaboration “Observation of a new boson at a mass of 125 GeV with the CMS experiment at the LHC” Phys. Lett. B716 (2012) 30-61

[11] Trimble, Virginia “Existence and nature of dark matter in the universe” Annual review of astronomy and astrophysics. Volume 25 (A88-13240 03-90). Palo Alto, CA, Annual Reviews, Inc., 1987, p. 425-472

[12] A. Sakharov, “Violation of CP Invariance, c Asymmetry, and Baryon Asymmetry of the Universe”, Pisma Zh.Eksp.Teor.Fiz. 5 (1967) 32.

[13] Y. Fukuda et al. (Super-Kamiokande Collaboration) “Evidence for Oscillation of Atmospheric Neutrinos”, Phys. Rev. Lett. 81, 1562-1567 (1998)

[14] Q. R. Ahmad et al. (SNO Collaboration) “Measurement of Day and Night Neutrino Energy Spectra at SNO and Constraints on Neutrino Mixing Parameters”, Phys. Rev. Lett. 89, 011302 (2002)

[15] http://scienceblogs.com/startswithabang/2013/05/15/the-rise-and-fall-of-supersymmetry/

[16] http://www.quantumdiaries.org/2012/7/page/6/

[17] Stephen P. Martin, “A Supersymmetry Primer” arXiv:hep-ph/9709356

[18] The CMS Collaboration, Search for supersymmetry in the all-hadronic final state using top quark tagging in pp collisions at $\sqrt{s} = 13$ TeV

[19] Barney, David “CMS Detector Slice”, CMS-PHO-GEN-2016-001

[20] “ROOT Reference Guide”, https://root.cern.ch/root/html534/ClassIndex.html

[21] CMS Collaboration, The CMS experiment at the CERN LHC JINST 3 (2008) S08004 doi:10.1088/1748-0221/3/08/S08004

[22] CMS Collaboration, “ParticleFlow Event Reconstruction in CMS and Performance for Jets, Taus, and E_T^{miss}”, CMS Physics Analysis Summary CMS-PAS-PFT-09-001, 2009.

[23] M. Cacciari, G. P. Salam, and G. Soyez, The anti-k t jet clustering algorithm, JHEP 0804:063 (2008) doi:10.1088/1126-6708/2008/04/063 arXiv:0802.1189.

[24] CMS Collaboration, Identification of b quark jets at the CMS Experiment in the LHC Run 2, CMS Physics Analysis Summary CMS-PAS-BTV-15-001, CERN, Geneva, 2016.

[25] CMS Experiment at LHC, CERN "Dimuon Top Quark Event" Data Recorded Sun July 18, 11:13:22 2010 CEST

[26] J. Alwall et al., MadGraph5: going beyond, JHEP 06 (2011) 128, doi:10.1007/JHEP06(2011)128, arXiv:1106.0522.

[27] T. Sjostrand, S. Mrenna, and P. Z. Skands, A Brief Introduction to PYTHIA 8.1, Comput.Phys. Commun. 178 (2008) 852867, arXiv:0710.3820.

[28] CMS Collaboration, Event generator tunes obtained from underlying event and multiparton scattering measurements, Eur. Phys. J. C76 (2016), no. 3, 155, doi:10.1140/epjc/s10052-016-3988-x, arXiv:1512.00815.

[29] NNPDF Collaboration, Parton distributions for the LHC Run II, JHEP 04 (2015) 040, arXiv:1410.8849.

[30] GEANT4 Collaboration, GEANT4a simulation toolkit, Nucl. Instrum. Meth. A 506 (2003) 250, doi:10.1016/S0168-9002(03)01368-8.

[31] http://www-d0.fnal.gov/Run2Physics/top/top_public_web_pages/top_feynman_diagrams.html

[32] C. Patrignani et al. (Particle Data Group), Chin. Phys. C, 40, 100001 (2016).

[33] Nicolas Kohler, "Search for top squarks using spin correlations with the ATLAS experiment" CERN-THESIS-2014-270.

[34] V. Khachatryan et al. (CMS Collaboration) "Measurements of $t\bar{t}$ spin correlations and top quark polarization using dilepton final states in pp collisions at $sqrts = 8$ TeV", Phys. Rev. D 93, 052007

[35] ATLAS Collaboration, G. Aad et al., Observation of spin correlation in $t\bar{t}$ events from pp collisions at $\sqrt{s} = 7$ TeV using the ATLAS detector, Phys. Rev. Lett. 108 (2012) 212001.

[36] Haipeng An and Lian-Tao Wang, “Opening up the compressed region of stop searches at 13 TeV LHC” arXiv:1506.00653

[37] T. Junk, Confidence Level Computation for Combining Searches with Small Statistics, Nucl. Instrum. Meth. A434 (1999) 435443, doi:10.1016/S0168-9002(99)00498-2, arXiv:hep-ex/9902006.

[38] A.L. Read (F. James, L. Lyons and Y. Perrin (eds.)). Modified Frequentist analysis of search results (the CLs method) - in Workshop on Confidence Limits, CERN, Yellow Report 2000-005 https://cds.cern.ch/record/451614/files/open-2000-205.pdf

[39] A. L. Read, Presentation of search results: The CL(s) technique, J. Phys. G 28 (2002) 2693, doi:10.1088/0954-3899/28/10/313.

[40] The ATLAS Collaboration, The CMS Collaboration, The LHC Higgs Combination Group “Procedure for the LHC Higgs boson search combination in Summer 2011”.

[41] The CMS Collaboration, “Search for direct top squark pair production in the dilepton final state at $\sqrt{s} = 13$ TeV” CMS PAS SUS-16-027